"Novel Drilling Technology Combining Hydro-Jet and Percussion for ROP Improvement in deep geothermal drilling"	This project has received funding from the European Union's Horizon 2020 research and innovation programme under grant agreement No 101006752

DELIVERABLE D6.1

"Bit-rock interface influence on the rock percussive breaking efficiency"

ABSTRACT

In this work, a continuum, isotropic elasto-visco-plastic, and damage-based model, also called the concrete damaged plasticity (CDP) model, available in Abaqus, has been calibrated, and used to study bit-rock interaction under representative deep downhole percussive conditions.
Red Bohus granite data were prioritized for the current study given the large amount of available experimental data (to calibrate and assess the model) and their (sufficiently small) grain size which make them more suitable for a continuum FEM approach.
Parametric investigations where therefore carried out to support the drill bit design and to evaluate how grooves, created with a HPWJ system on the bottom-hole, can contribute to improve the down-hole percussive performance in granite.
It is shown that a drill bit with a combination of conical and spherical inserts is more efficient with respect to rock removal when compared to a drill bit made of only spherical inserts.
The study shows also that flat and concave geometries are the most efficient with respect to rock removal. Impact energy has a strong influence on rock removal while weight-on-bit has little effect. Furthermore, the effect of drilling depth shows lower rock removal for higher depths, due to higher confining pressure.

Disclaimer

DOCUMENT TYPE	Report
DOCUMENT NAME:	ORCHYD_Deliverable D 6.1_Bit-rock-interaction
VERSION:	vfinal
DATE:	02/02/2024
STATUS:	S0
DISSEMINATION LEVEL:	PU

AUTHORS, REVIEWERS				
AUTHOR(S):	Stéphane Dumoulin, Alexandre Kane			
AFFILIATION(S):	SINTEF Industry			
FURTHER AUTHORS:				
PEER REVIEWERS:	Laurent Gerbaud, John-Paul Latham			
REVIEW APPROVAL:	Approved	Yes	Rejected (to be improved as indicated below)	No
REMARKS / IMPROVEMENTS:				

VERSION HISTORY			
VERSION:	DATE:	COMMENTS, CHANGES, STATUS:	PERSON(S) / ORGANISATION SHORT NAME:
v0.1	08/12/2023	First draft	Stéphane Dumoulin (SINTEF)
v1.1	02/01/2024	First review	John-Paul Latham (ICL) and Laurent Gerbaud (ARMINES)
v2.1	15/01/2024	Second draft	Stéphane Dumoulin (SINTEF)
v3.1	22/01/2024	Second review	John-Paul Latham (ICL)
vfinal	26/01/2024	Final version	Stéphane Dumoulin (SINTEF)

VERSION NUMBERING	
v0.x	draft before peer-review approval
v1.x	After the first review
v2.x	After the second review
vfinal	Deliverable ready to be submitted!

STATUS / DISSEMINATION LEVEL			
STATUS		DISSEMINATION LEVEL	
S0	Approved/Released/Ready to be submitted	**PU**	Public
S1	Reviewed	**CO**	Confidential, restricted under conditions set out in the Grant Agreement
S2	Pending for review		
S3	Draft for comments	**CI**	Classified, information as referred to in Commission Decision 2001/844/EC.
S4	Under preparation		

TABLE OF CONTENTS

1 Introduction 4

2 Selected granite 4

  2.1 The different granites 4

  2.2 Description of selected granite 6

3 Rock model for dynamic indentation 6

  3.1 Description of the model 6

  3.2 Calibration and validation of the indentation model 9

    3.2.1 Rock bulk experimental tests 9

    3.2.2 Material model calibration 10

    3.2.3 Effect of insert shape 15

    3.2.4 Inserts interaction distance study 16

4 Drill bit-rock interaction 17

  4.1 Drill bit inserts shape 18

  4.2 Effect of bottom hole geometry 20

  4.3 Simulation loading hypotheses 29

  4.4 Effect of drilling operating conditions 31

  4.5 Effect of bottom hole geostatic conditions 32

  4.6 Computational aspects 33

5 Conclusions 33

References 34

Appendix A. Effect of mesh size 36

Appendix B. Effect of heterogeneity 38

CONTENT

1 Introduction

This study is performed in the context of the EU project ORCHYD (2021), where an innovative drilling tool, combining high pressure water jetting and percussive drilling, is developed to increase hard rock drilling rates in deep geothermal wells.

The role, at the bit-rock interaction, of the downhole loading and contact conditions on the hard rock percussive breaking efficiency has been investigated in various experimental and numerical studies. These studies have highlighted in particular the decrease of rock breaking efficiency and rate of penetration (ROP) with an increase of confining pressure, the nonlinear (with a tendency to saturation) effect of an increasing impact energy on the rock breaking efficiency and the potential increase of the mechanical specific energy from a flat surface (limiting the number of buttons impacting the rock) to a parabolic surface [1]-[6]. However, the potential use of high-pressure water jetting (HPWJ), at the bit-rock interaction, release stresses at the cutting face that can improve the percussive drilling efficiency remains poorly explored.

In this study we have numerically investigated how grooves, created with a HPWJ system on the bottom-hole, can contribute to improve the down-hole percussive performance in granite.

This was achieved by performing single drill bit impact simulations (3D) under representative deep drilling conditions. The pressure and rate dependency of the rock behaviour and breaking process see [7]-[9], are captured with use of an elasto-plastic and damage model for hard rock (Concrete Damage Plasticity model in Abaqus), calibrated against uniaxial compression static tests and triaxial static tests done on the selected Red Bohus (compressive tests with confining pressure varying from 0 to 100 MPa). While pressure sensitivity is calibrated using tests performed in ORCHYD, strain-rate sensitivity is obtained using data from the literature.

Parametric finite element (FE) simulations were therefore conducted in order to assess the influence of various bit designs and bottom hole profiles on the rock breaking efficiency. Four different bit geometries were modelled (flat, parabolic, pure-parabolic and concave) with their associated bottom hole profiles (assuming idealized surfaces at steady state conditions) and by considering various peripheral groove depths (3 mm wide groove with 3 depths: 0, 10, 30 mm). The effect of depth, impact energy, weight-on-bit, insert shape and stress release were investigated.

2 Selected granite

2.1 The different granites

Three granites have been studied in ORCHYD, i.e., Sidobre, Red Bohus and Kuru Grey. Kuru Grey outcrops in Finland, Red Bohus in Sweden and Sidobre in South of France. Kuru Grey granite belongs to the Paleoproterozoic Svecofennian orogenic belt (1930-1800 million years) and Red Bohus to the late stage of the Svecon준vegian orogen (900 Myr). They are both parts of the oldest outcropping rocks in northern Europe. Sidobre granite belongs to the Variscan chain which forms a major part of bedrock of central and southern Europe (the Variscan orogeny ended in the Permian age, 250 Myr ago). For granite rocks, the average grain size is used to define three rock categories: fine (<1 mm), medium (1-5 mm) and coarse (>5 mm). As the size of the drilling tools used in the ORCHYD project are in the range of such grain sizes, a granite of each category was selected to assess the effect of these dimensions on the drilling efficiency: Kuru Grey, Red Bohus and Sidobre are fine-, medium- and coarse-grained, respectively.

In an ongoing publication [10], different experimental tests performed on the three rocks, from both studies unrelated to and related to the ORCHYD project, are gathered. The test data include Uniaxial Compressive Strength (UCS), Brazilian Tensile Strength (BTS) tests and triaxial compressive strength tests with confining pressures up to 225 MPa or/and high strain-rates up to 10^3/s. Figure 1(a) and (b) show the differential peak stress versus confining pressure and the dynamic increase factor (DIF) versus strain-rate, relatively; the DIF is defined as the ratio between the peak stress at atmospheric pressure at any strain-rate, to the peak stress at atmospheric pressure and at low strain-rate. These test results show that the effect of confining pressure and strain-rate on compressive strength are uncoupled. These effects are then estimated independently, and a fracture criterion accounting for both variables is proposed for the family of very hard granites.

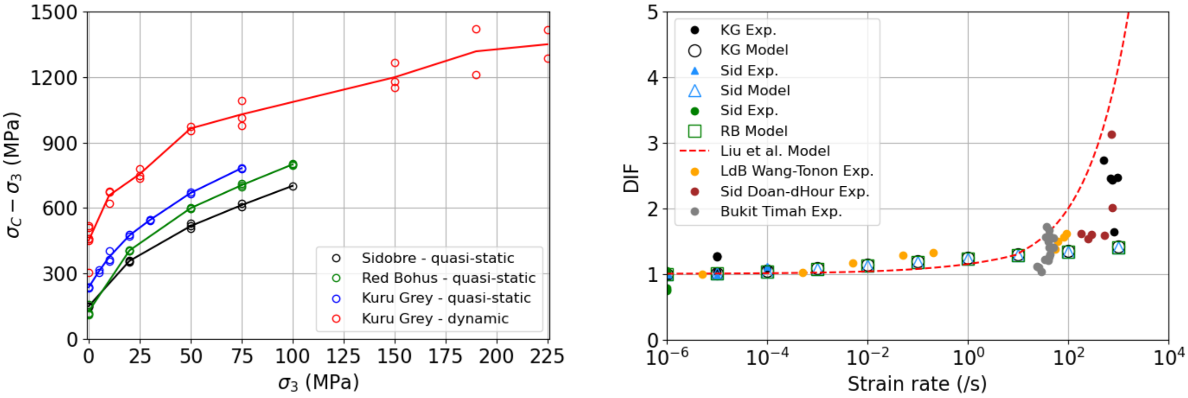

(a) (b)

Figure 1: (a) Differential peak stress ($\sigma_C - \sigma_3$) versus confining pressure σ_3 for the three granites; σ_C is the peak axial stress. The solid lines go through the average differential peak stress for each confining pressure. The curves are almost parallel to each other (i.e. the effect of confining pressure is independent of the strain-rate), (b) DIF versus strain-rate for experiments on Kuru Grey, Sidobre and Red Bohus from the current study, and data from the literature; results from the proposed model and from the model proposed by Liu et al. [11] are also included. The two plots are extracted from [10].

These test data revealed that all three granites exhibit a similar non-linear pressure (for pressures higher than about 20 MPa), Figure 1(a), and strain-rate dependence, Figure 1(b), when considering the rock bulk material, i.e., the specimen size (the number of grains) makes it possible to capture representative rock bulk behaviour. This appears convenient for the purpose of our current parametric study, where a continuum damage approach is selected for the parametrical FEM study, to provide a representative trend of the rock granite breaking efficiency. However, at the insert-rock interaction scale, the large grain size of Sidobre makes a continuum approach dubious, although some large feldspars grains may be present in Red Bohus. For more consistency and considering the large data set available through the work of Aldannawy et al. [12] for Red Bohus, this granite (with smaller gains than Sidobre) was selected for the rock model calibration, where both insert-rock data and rock bulk behaviour data are used.

Note that the effect of grain size heterogeneities at the bit-rock interaction is addressed in a separate study that will be part of another deliverable. An example is however shown in Appendix B.

2.2 Description of selected granite

Red Bohus is extracted near the cities of Brastad and Lysekil in Sweden. The batholith dates from 922 million years, is 100 km long and 22 km wide [13]. Red Bohus granite is a light reddish rock, with interlocking crystal grains, composed of feldspar (white or pink in Figure 2(a)) of the order of 60wt%, quartz (grey) of the order of 35wt% and biotite (black) of the order of 5wt%. Feldspars have sizes that can be larger than several millimetres. Iron oxides coloured feldspar minerals in orange. No anisotropy is observable.

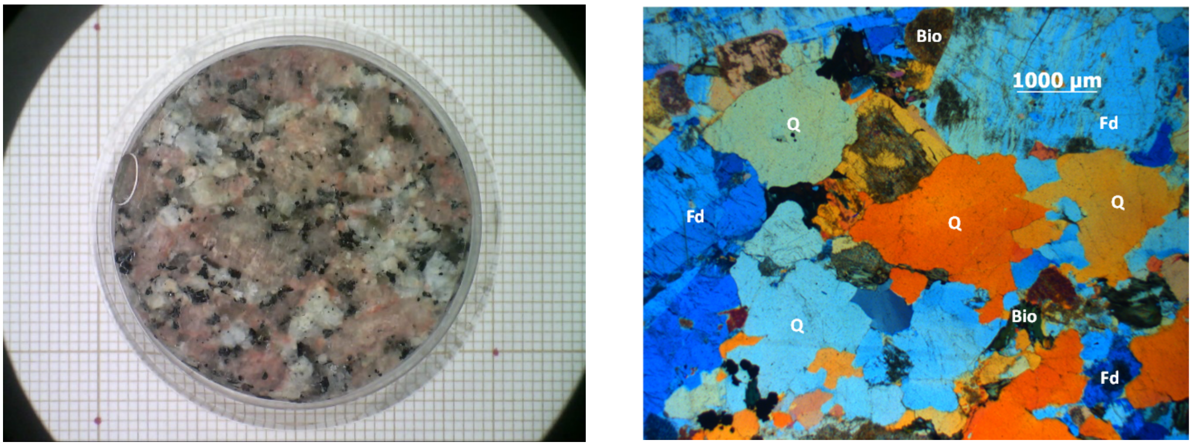

(a) (b)

Figure 2: (a) Macroscopic view and (b) representative microscope observations of grain size and structure under cross polarized light for Red Bohus granite.

3 Rock model for dynamic indentation

3.1 Description of the model

The model used is a damaged plasticity model for concrete and other quasi-brittle materials, also called the concrete damaged plasticity (CDP) model, available in Abaqus. It will be briefly described here but an interested reader may look at the detailed description in the documentation of Abaqus [14].

The CDP model is a continuum, isotropic elasto-visco-plastic, and damage-based model. It is based on the assumption that the failure mechanisms are tensile cracking and compressive crushing. The degradation of the material is therefore characterised by two independent damage variables, one in tension, d_t, and another in compression, d_c, which in turn depend on two hardening variables, in tension and compression, $\tilde{\varepsilon}_t^p$ and $\tilde{\varepsilon}_c^p$, respectively. In the following, subscript *t* and *c* refer to variables in tension and compression, respectively.

In this plastic-damage model, the effective stress tensor $\bar{\boldsymbol{\sigma}}$, i.e., that relates to the area effectively resisting external load, is defined as:

$$\bar{\boldsymbol{\sigma}} = \mathbf{D}_0^{\mathrm{e}} : (\boldsymbol{\varepsilon} - \boldsymbol{\varepsilon}^{\mathrm{p}}) \tag{1}$$

where $\mathbf{D}_0^e$ is the initial, or undamaged, elastic stiffness tensor, $\boldsymbol{\varepsilon}$ is the total strain tensor and $\boldsymbol{\varepsilon}^p$ is the plastic strain tensor. The Cauchy stress tensor then reads:

$$\boldsymbol{\sigma} = (1-d)\bar{\boldsymbol{\sigma}}; \quad 1 \leq d \leq 0 \tag{2}$$

where d is the scalar degradation, or stiffness reduction, variable.

The hardening variables $\tilde{\varepsilon}_t^p$ and $\tilde{\varepsilon}_c^p$ depend on the plastic part $\dot{\boldsymbol{\varepsilon}}^p$ of the strain rate $\dot{\boldsymbol{\varepsilon}}$ through:

$$\dot{\tilde{\boldsymbol{\varepsilon}}}^p = \mathbf{h}(\hat{\bar{\boldsymbol{\sigma}}}, \tilde{\boldsymbol{\varepsilon}}^p).\hat{\dot{\boldsymbol{\varepsilon}}}^p \tag{3}$$

with

$$\dot{\tilde{\boldsymbol{\varepsilon}}}^p = \begin{bmatrix} \dot{\tilde{\varepsilon}}_t^p \\ \dot{\tilde{\varepsilon}}_c^p \end{bmatrix}; \quad \hat{\dot{\boldsymbol{\varepsilon}}}^p = \begin{bmatrix} \hat{\dot{\varepsilon}}_1^p \\ \hat{\dot{\varepsilon}}_2^p \\ \hat{\dot{\varepsilon}}_3^p \end{bmatrix}; \quad \tilde{\boldsymbol{\varepsilon}}^p = \int_0^t \dot{\tilde{\boldsymbol{\varepsilon}}}^p dt \tag{4}$$

and

$$\mathbf{h}(\hat{\bar{\boldsymbol{\sigma}}}, \tilde{\boldsymbol{\varepsilon}}^p) = \begin{bmatrix} r(\hat{\bar{\boldsymbol{\sigma}}}) & 0 & 0 \\ 0 & 0 & -[1 - r(\hat{\bar{\boldsymbol{\sigma}}})] \end{bmatrix} \tag{5}$$

where the stress weight factor $r(\hat{\bar{\boldsymbol{\sigma}}})$ reads:

$$r(\hat{\bar{\boldsymbol{\sigma}}}) = \frac{\sum_{i=1}^{3} \langle \hat{\bar{\sigma}}_i \rangle}{\sum_{i=1}^{3} |\hat{\bar{\sigma}}_i|} \tag{6}$$

where $\hat{\mathbf{X}}$ refers to the principal components, or eigenvalues, of tensor $\mathbf{X}$ and $\langle . \rangle$ is the Macauley bracket. Note that $\hat{X}_1$, $\hat{X}_2$ and $\hat{X}_3$ are, respectively, the maximum, intermediate and minimum eigenvalue.

The scalar degradation variable d is defined as follows:

$$(1-d) = (1 - s_t d_c)(1 - s_c d_t), \quad 0 \leq s_t, \quad s_c \leq 1 \tag{7}$$

with

$$\begin{aligned} s_t &= 1 - w_t r(\hat{\bar{\boldsymbol{\sigma}}}); \quad 0 \leq w_t \leq 1 \\ s_c &= 1 - w_c[1 - r(\hat{\bar{\boldsymbol{\sigma}}})]; \quad 0 \leq w_c \leq 1 \end{aligned} \tag{8}$$

w_t and w_c are weight factors that control the recovery of the stiffness in tension and compression upon load reversal. For example, to reproduce experimental observations of crack closure when the load is reversed from tension to compression, i.e., that the compressive stiffness is fully recovered, set $w_c = 1$. However, changing load from compression to tension, crushing cracks remain, the tensile stiffness will not be recovered, i.e., $w_t = 0$.

The yield function from Lubliner et al. [15] and modified by Lee and Fenves [16] is adopted:

$$F(\bar{\boldsymbol{\sigma}}, \tilde{\boldsymbol{\varepsilon}}^p) = \frac{1}{1-\alpha}\left[\bar{q} - 3\alpha\bar{p} + \beta(\tilde{\boldsymbol{\varepsilon}}^p)\langle\bar{\sigma}_1\rangle - \gamma\langle-\bar{\sigma}_1\rangle\right] - \bar{\sigma}_c\left(\tilde{\varepsilon}_c^p\right) \tag{9}$$

where $\bar{\sigma}_c\left(\tilde{\varepsilon}_c^p\right)$ is the effective flow stress in compression.

$$\bar{p} = -\frac{1}{3}\bar{\boldsymbol{\sigma}}:\mathbf{I} \tag{10}$$

is the effective hydrostatic pressure,

$$\bar{q} = \sqrt{\frac{3}{2}\bar{\mathbf{S}}:\bar{\mathbf{S}}} \tag{11}$$

is the von Mises equivalent effective stress, and

$$\bar{\mathbf{S}} = \bar{p}\mathbf{I} + \bar{\boldsymbol{\sigma}} \tag{12}$$

is the deviatoric stress tensor and $\mathbf{I}$ is the identity tensor.

It is reminded that $\bar{\sigma}_1$ is the maximum principal stress of $\bar{\boldsymbol{\sigma}}$. The coefficient α depends on the ratio of initial equibiaxial compressive yield stresses to initial uniaxial compressive yield stress, σ_{b0} and σ_{c0}, respectively, as:

$$\alpha = \frac{\sigma_{b0}/\sigma_{c0} - 1}{2\,\sigma_{b0}/\sigma_{c0} - 1} \tag{13}$$

The function $\beta(\tilde{\boldsymbol{\varepsilon}}^p)$ writes:

$$\beta = \frac{\bar{\sigma}_c\left(\tilde{\varepsilon}_c^p\right)}{\bar{\sigma}_t\left(\tilde{\varepsilon}_t^p\right)}(1-\alpha) - (1+\alpha) \tag{14}$$

with $\bar{\sigma}_t\left(\tilde{\varepsilon}_t^p\right)$ and $\bar{\sigma}_c\left(\tilde{\varepsilon}_c^p\right)$ the effective tensile and compressive cohesion stress, respectively.

The coefficient γ writes:

$$\gamma = \frac{3(1-K_c)}{2K_c - 1} \tag{15}$$

where K_c is the ratio of the second stress invariant on the tensile median to the second stress invariant on the compressive median, at initial yield for any given value of the pressure $\bar{p}$, such that the maximum principal stress is negative.

Finally, the CDP model uses a non-associated potential flow:

$$\dot{\boldsymbol{\varepsilon}}^p = \dot{\lambda}\frac{\partial G(\bar{\boldsymbol{\sigma}})}{\partial \bar{\boldsymbol{\sigma}}} \tag{16}$$

where $\dot{\lambda}$ is the plastic parameter and the flow potential G is the Drucker-Prager hyperbolic function:

$$G(\bar{\boldsymbol{\sigma}}) = \sqrt{(\epsilon\sigma_{t0}\tan\psi)^2 + \bar{q}^2} - \bar{p}\tan\psi \tag{17}$$

where σ_{t0} is the uniaxial tensile stress at failure or cracking stress, ψ is the dilation angle and ϵ is the eccentricity defining the rate at which $G(\bar{\boldsymbol{\sigma}})$ approaches the asymptote.

The conditions for elastic loading and unloading follow the Kuhn-Tucker condition:

$$\dot{\lambda}\, F(\bar{\boldsymbol{\sigma}}, \tilde{\boldsymbol{\varepsilon}}^{p}) = 0, \quad F(\bar{\boldsymbol{\sigma}}, \tilde{\boldsymbol{\varepsilon}}^{p}) \leq 0, \quad \dot{\lambda} \geq 0 \tag{18}$$

The parameters provided to Abaqus to define the CDP model are the dilation angle ψ, the eccentricity ϵ, the ratio of initial equibiaxial to initial uniaxial compressive yield stress σ_{b0}/σ_{c0} and the ratio of the second stress invariants on the tensile and compressive meridians K_c.

Furthermore, the hardening behaviour in tension and compression must be provided as tabulated data of tensile and compressive stress as function of cracking tensile, $\tilde{\varepsilon}_t^{ck}$, and inelastic compressive, $\tilde{\varepsilon}_c^{in}$, strain, respectively. These strain variables can be easily related to the plastic strains as:

$$\begin{aligned} \tilde{\varepsilon}_t^{p} &= \tilde{\varepsilon}_t^{ck} - \frac{d_t}{1 - d_t}\frac{\sigma_t}{E_0} \\ \tilde{\varepsilon}_c^{p} &= \tilde{\varepsilon}_c^{in} - \frac{d_c}{1 - d_c}\frac{\sigma_c}{E_0} \end{aligned} \tag{19}$$

where E_0 is the undamaged Young's modulus and, σ_t and σ_c are the stress in tension and compression, respectively. In tension, the hardening can also be defined as cracking stress as function of the cracking displacement, instead of strain, or failure stress as function of fracture energy.

To obtain a fully coupled plastic-damage model, the evolution of the damage variables in tension, d_t, and in compression, d_c, must be provided as tabular functions of the cracking and inelastic strain, respectively. Concerning the behaviour in tension, the damage can be also defined as function of cracking displacement.

Finally, rate dependence can be introduced by defining the hardening behaviour in tension and compression as tabular functions of the cracking and inelastic strain rate. Note that the evolution of damage cannot be defined as function of the strain rate, i.e., it is assumed being rate independent.

3.2 Calibration and validation of the indentation model

3.2.1 Rock bulk experimental tests

Uniaxial compression tests were performed on Red Bohus specimens with a diameter of 50 mm and a height of 100 mm. The specimens were then compressed parallel to their longitudinal axis until a strain of about 5% with a constant axial strain rate of 60 μm/m/min. Triaxial tests were also performed on specimens with a diameter of 40 mm and a height of 100 mm, with four confining pressures, 20, 50, 75 and 100 MPa. All specimens were tested dry, i.e., conditioned to room humidity, and at room temperature, approx. 23 °C. Brazilian tests were also performed on specimens with a diameter of 50 mm and a height of 25 mm at a loading rate of 200 N/s. The stress versus axial and radial strains for Brazilian and triaxial tests are shown in Figure 3.

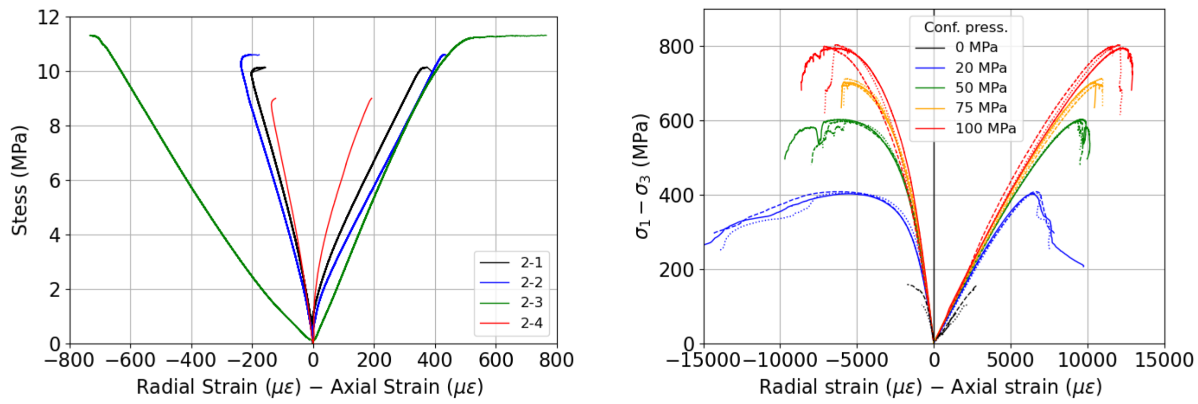

(a) (b)

Figure 3: (a) Stress versus axial and radial strains from Brazilian tests and (b) differential stress versus axial and radial strains for different confining pressures from triaxial tests; σ_1 is the axial stress and σ_3 the confining pressure; the different lines with the same colour represent test repetitions.

3.2.2 Material model calibration

3.2.2.1 Hardening, flow potential and yield surface

At first the response of the material to uniaxial loading in tension and compression is defined. As can be seen in Figure 3(b), the compression curve (0 MPa) does not have any softening response, i.e., the sample broke just after the peak. The stress versus strain in compression was therefore obtained by using the response at 20 MPa confining pressure and scaled down to have the same peak as at 0 MPa confining pressure. The response in tension was based on the Brazilian tests where the post-peak behaviour was defined to have a shape similar to that in compression. The curves thus obtained are shown in Figure 4. Eq. (19) was then used to obtain the tabulated tensile and compressive stress versus cracking and inelastic strain, as required by Abaqus.

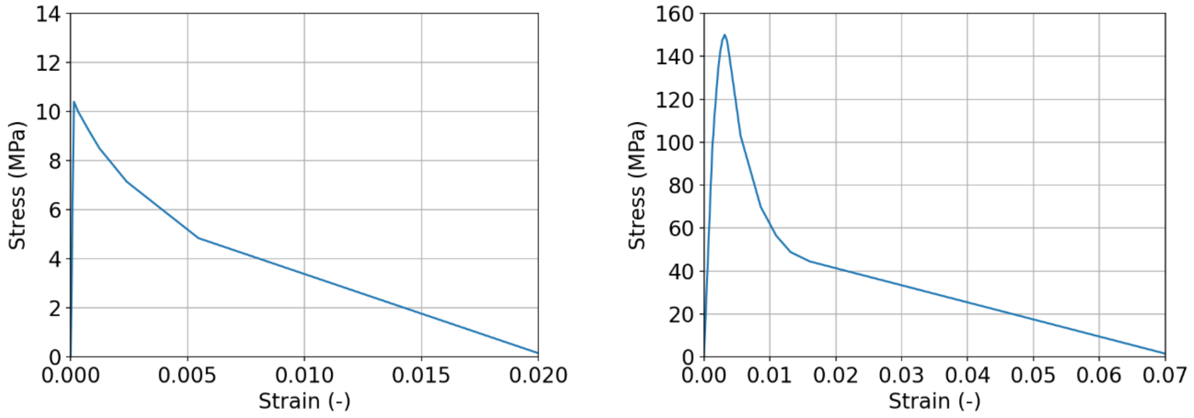

(a) (b)

Figure 4: Response of the material to uniaxial loading in (a) tension and (b) compression.

Under uniaxial conditions, the damage parameter can be defined as

$$d = 1 - \frac{E}{E_0} \tag{20}$$

where E is the damaged Young's modulus of the material.

Therefore, ideally, the damage parameter should be determined from a material test with loading/unloading cycles. In the absence of such data, it can be approximated as

$$d_t = 1 - \frac{\sigma_t}{\sigma_{t0}}; \qquad d_c = 1 - \frac{\sigma_c}{\sigma_{c0}} \tag{21}$$

Eq. (21) has been used to determine the damage parameter from each of the hardening curves shown in Figure 4. Note that this assumption results in elastic strains at any flow stress being equal to the elastic strain at initial yielding.

The model parameters related to the flow potential and yield surface – ψ, ϵ, σ_{b0}/σ_{c0} and K_c – are calibrated against the experimental quasi-static uniaxial compression and triaxial tests described above using a single element model. The model represents a rock sample with a 50 mm diameter and a length of 100 mm, using an axisymmetric element (CAX4R). The optimization software LS-OPT [17] was used for that purpose. The parameters thus obtained after calibration are given in Table 1 and the material response from the model against experiments for triaxial tests with different confining pressures is shown in Figure 5.

Table 1: Concrete damaged plasticity model parameters.

Young's modulus	76750 MPa		Eccentricity	0.38
Poisson coefficient	0.25		σ_{b0}/σ_{c0}	1.58
Density	2.62×10^{-9} N/mm^3		K_c	0.63
Dilation angle	35°		d_{crit}	0.85

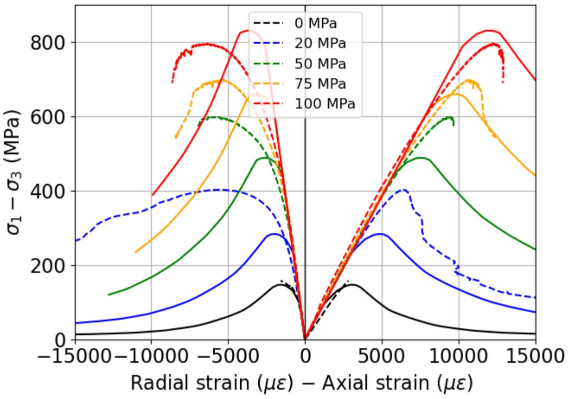

Figure 5: Differential stress versus axial and radial strains for different confining pressures from triaxial tests from model (solid lines) and experiments (dashed lines).

3.2.2.2 Strain-rate sensitivity

The strain-rate sensitivity was included in the model based on the work of Liu et al. [11] on dynamic increase factors (DIF). The research partner ICL extracted all data related to hard granites from Liu et al. [11] and derived the following semi-empirical equations. Based on the results shown in Figure 1(b), a threshold has been introduced at a DIF of about 2 to avoid unrealistic high strength for very large strain rates reached during the dynamic impact events of indentation or percussive drilling. This is confirmed in an ongoing study from the ORCHYD project [10].

The DIF in tension reads:

$$\begin{cases} \dot{\varepsilon} \leq 5 \times 10^{-6} & DIF = 1 \\ 5 \times 10^{-6} < \dot{\varepsilon} \leq 10^{2} & DIF = 0.95 + 0.41\dot{\varepsilon}^{0.17} \\ \dot{\varepsilon} > 10^{2} & DIF = 1.85 \end{cases} \tag{22}$$

The DIF in compression reads:

$$\begin{cases} \dot{\varepsilon} \leq 5 \times 10^{-6} & DIF = 1 \\ 5 \times 10^{-6} < \dot{\varepsilon} \leq 10^{4} & DIF = 0.77 + 0.56\dot{\varepsilon}^{0.07} \\ \dot{\varepsilon} > 10^{4} & DIF = 1.84 \end{cases} \tag{23}$$

3.2.2.3 Critical damage under dynamic indentation

The critical damage d_{crit}, or critical scalar degradation, Eq. (7), was calibrated using dynamic indentation tests with a single insert on Red Bohus performed by Aldannawy et al. [18]. The test set-up was modelled in Abaqus. The impact bar was modelled with 25744 C3D4 elements and the rock with 128000 C3D8R and 211057 C3D4 elements (see Figure 6). The insert, which had a conical shape with a radius of 4.2 mm and an angle of 60° (see Fig. 8 in [18]), was modelled as elastic with a Young's modulus of 630 GPa, a density of 1.28×10^{-8} N/mm^3 and a Poisson coefficient of 0.22 – tungsten carbide; the impact bar was modelled as elastic with a Young's modulus of 210 GPa, a density of 7.03×10^{-8} N/mm^3 and a Poisson coefficient of 0.27 – steel. The rock was modelled with the CDP model using the parameters given in Table 1. The rock was modelled with a 100 mm long, 80 mm wide and 50 mm high block.

In the experiments the impact bar is hit by a loading platen, or impactor, dropped from a given height [18]. This was modelled by using a connector element between two reference points, one connected to the upper surface of the impact bar, and one located above. The latter was given the same weight as the impactor in the experiments, and an initial velocity corresponding to the impact velocity of the impactor. The behaviour of the connector element was described by an axial non-linear elastic tabulated force versus displacement law which was obtained from a prior model of the whole mass-impact set-up. The force shown is the normal force due to contact pressure at the insert-rock interface while the displacement is taken at the node located at the tip of the insert. The accuracy of this representation is validated by comparing the force versus penetration curves, Figure 7(b), for two models, one using the connector element, Figure 6(a), and one where the impactor is explicitly accounted for, Figure 7(a). The force versus displacement curve reveals that there are several drops in load due to the different impacts between impactor and impact bar and bar and rock. The impactor hits the impact bar a first time. The latter hits the rock and then bounces back, i.e., the load and displacement decrease (first drop after a displacement of 1.5 mm). The impact bar then meets the impactor once more, while still slightly in contact with the rock, and penetrates even more in the rock. Finally, the impact bar bounces back and totally unloads the rock.

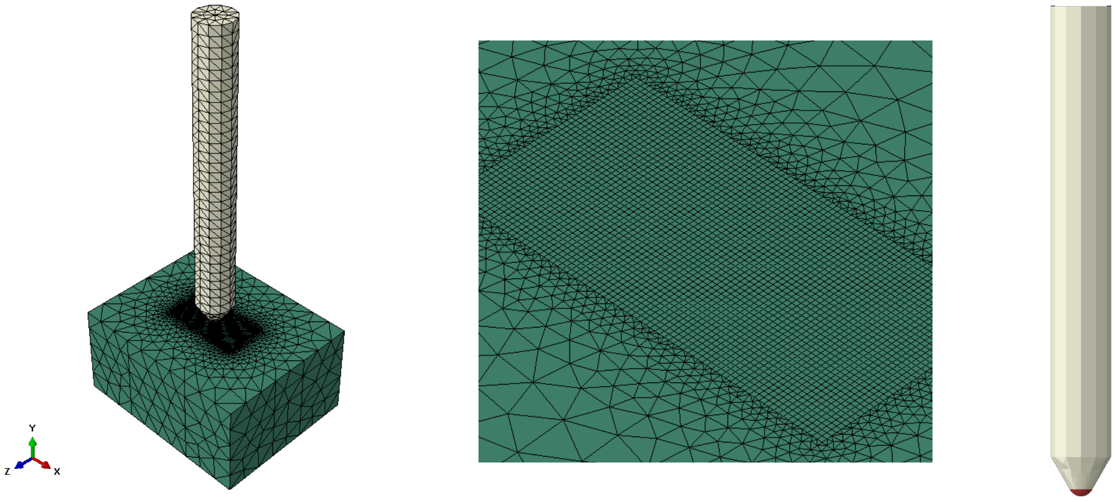

(a) (b) (c)

Figure 6: (a) Mesh of the whole model, (b) zoom on the finer mesh under the insert, (c) impact bar with insert (red colour).

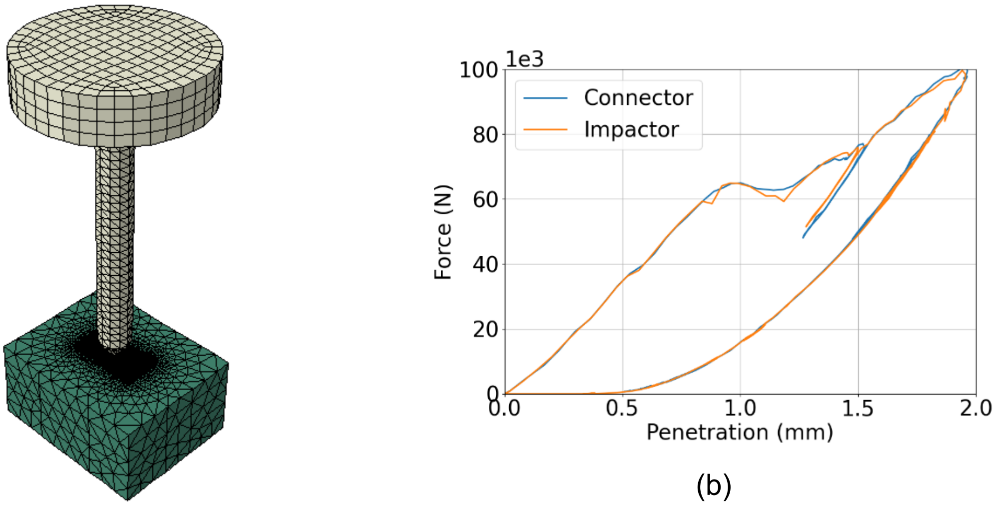

(a) (b)

Figure 7: (a) Mesh of the whole model including the impactor, (b) comparison of force versus penetration curves between the model with impactor and the model using a connector element.

The boundary conditions for the model were the same as in the experiments: a confining pressure of 30 MPa was applied to all faces of the rock, and a constant pressure was applied on the top face of the impact bar to give a weight-on-bit of 2.88 kN. The bottom plane of the rock ((XZ) plane in Figure 6(a)) was fully constrained. Simulations were run for different impact energies, 30, 40, 50, 60, 74, 94 and 114 J. The removed volume was computed by summing the volume of all elements with a critical damage higher than a given value. Different values for d_{crit} were chosen to find an optimum value. The results obtained are shown in Figure 8 where the numerical results are compared with the experimental data from [18]. It appears that a critical damage between 0.85 and 0.9 provides good results, see Figure 8. Impact energies in real drilling conditions tend to be above 50/60 J per insert, Furthermore, the investigations in the remainder of this study will be performed for impact values of about 60 J per insert. Noting also that there are some outliers at 60, 74 and 114 J, a critical damage value of 0.85 is therefore chosen.

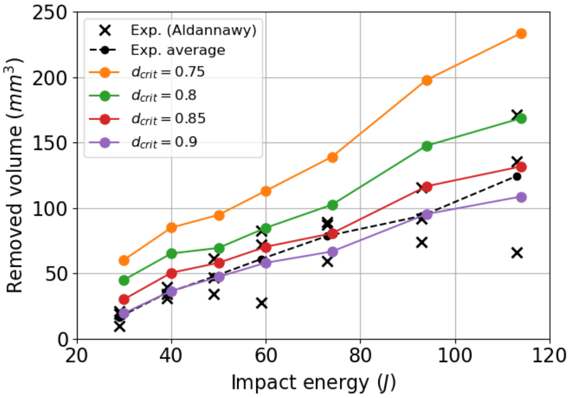

Figure 8: Removed volume versus impact energy from experiments [18], dark crosses, and modelling (solid lines); the dash line is the averaged experimental data.

Figure 9 shows the contour plots for the accumulated damage, or scalar degradation, see Eq. (7), and damage in tension, in the rock after impact, corresponding to impact energies of 30 J and 114 J. Sub-figures (a) to (d) show the damage in a cross-section of the rock in the plane containing the axis of the impact bar. The damage in compression is not shown as it would appear as identical to the accumulated damage. A deeper indent, a generally larger damaged volume, and a larger damaged volume above the critical damage, are observed for a higher impact energy, as expected.

Figure 10 shows the force versus penetration curves for each impact energy considered. There is a clear trend of increase in force and penetration with the impact energy. The permanent penetration, i.e., displacement after unloading, increases with the impact energy: this indicates that the indent depth, and thereby damage as shown in Figure 8, increase with impact energy.

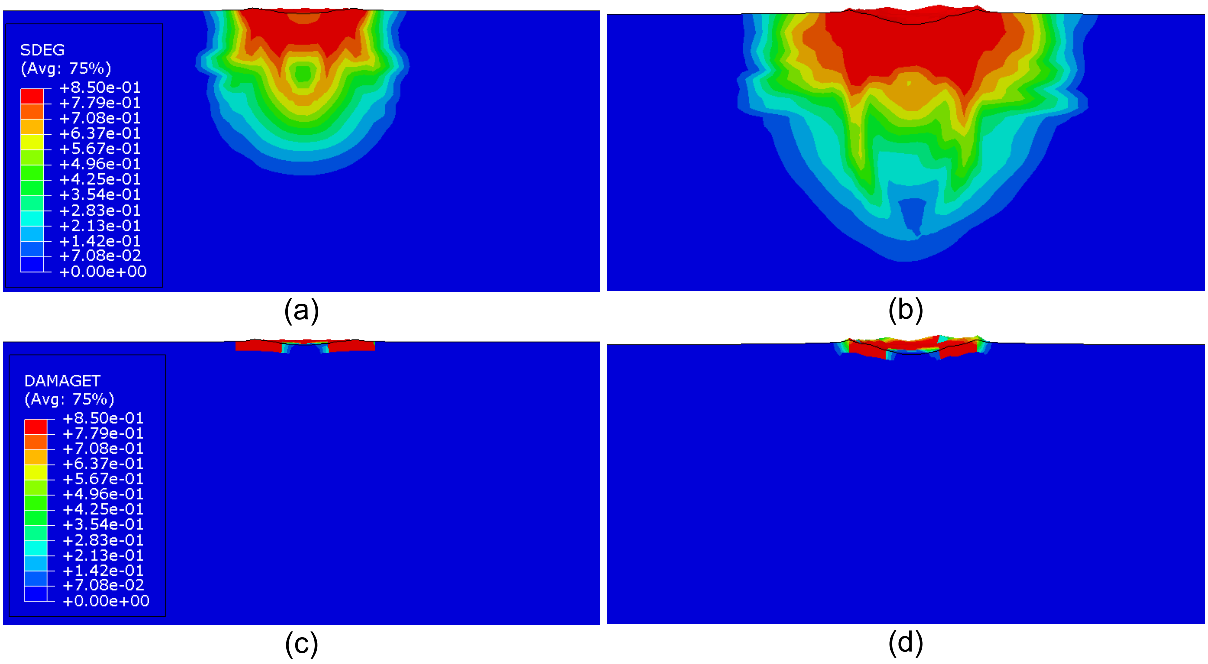

(a) (b)

(c) (d)

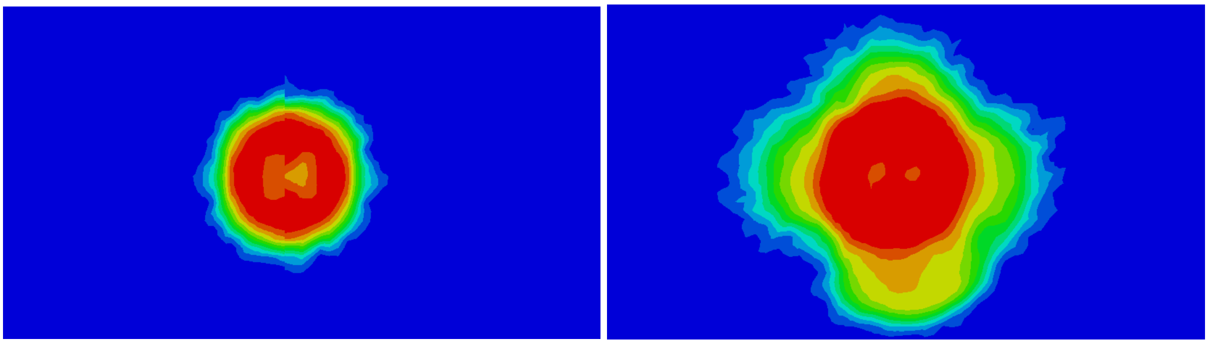
(e) (f)

Figure 9: Cross-section of the rock in the plane containing the axis of the impact bar, showing damage contour plots under the insert after impact. (a)-(b) Scalar degradation and (c)-(d) damage in tension. (a)-(c) Contour plots for impact energy of 30 J and (b)-(d) for an impact energy of 114 J. (e)-(f) Same as (a)-(b) seen from above; same contour scale applies. The grey colour shows damage higher than the critical damage, i.e., 0.85; the black lines in the grey zones are the feature edges.

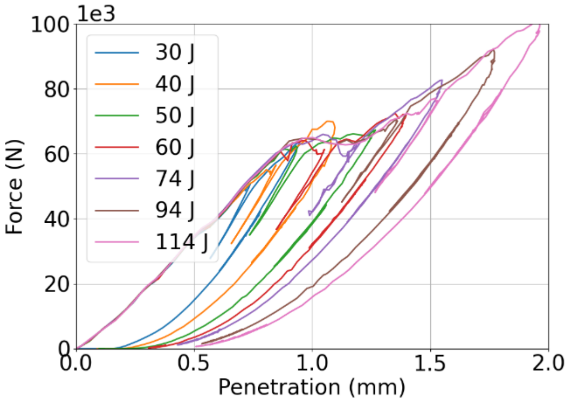

Figure 10: Impact force versus penetration for the different impact energies considered.

3.2.3 Effect of insert shape

It has been shown experimentally that insert shape affects stress distribution during impact and thereby affects rock removal, see Aldannawy [12]. The same model as the one described in the previous section has been used. The simulations were run for three different insert shapes, the conical one, as used in the previous section, and two spherical ones, a so-called S13, with a radius of 6.5 mm, and another spherical insert, S16, with a radius of 8 mm, see [12]. A confining pressure of 30 MPa and an impact energy of 60 J were used.

Figure 11 shows the contour plots for the accumulated damage, or scalar degradation, see Eq. (7), and damage in tension, in a cross-section of the rock in the plane containing the axis of the impact bar, corresponding to the insert geometries. A deeper indent is observed for the conical insert while a broader damaged area is observed for the spherical inserts. The volume removed were 70.25, 59.25 and 55.625 for the conical, S13 and S16 insert, respectively. This trend is identical to the experimental observations. The damage goes deeper in the rock with the spherical inserts than with the conical one and the shape of the damage distribution is more round with the former than with the conical insert. However, the damage higher than 0.85 goes deeper into the rock for the conical insert. Furthermore, the damage in tension higher than 0.85 (red colour) is larger for the spherical inserts than the conical one. In conclusion, a higher and deeper volume of rock is removed with the conical insert while a larger and deeper volume is damaged, but not removed, with spherical inserts.

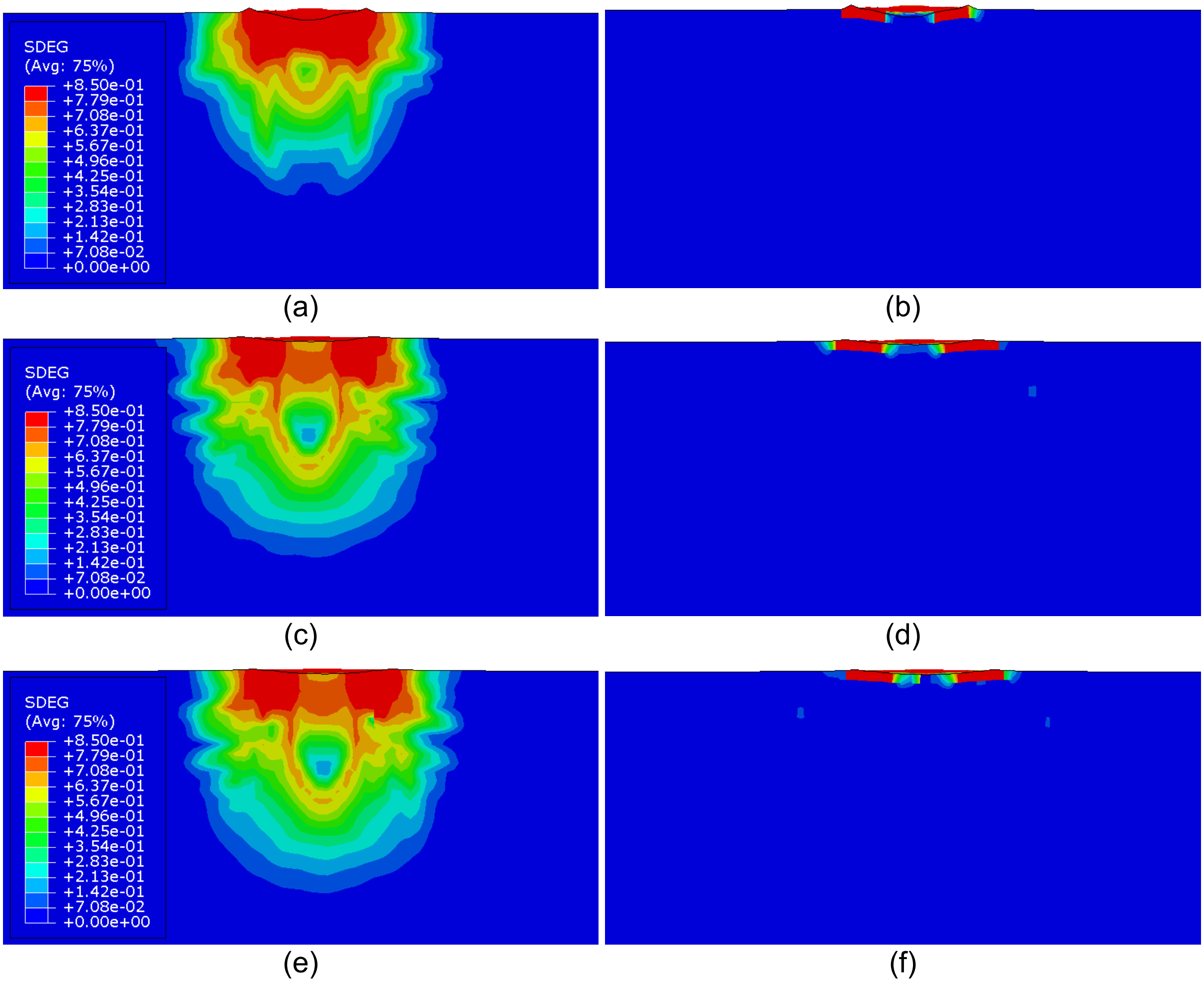

Figure 11: Cross-section of the rock in the plane containing the axis of the impact bar, showing damage contour plots under the insert after impact. (a)-(c)-(e) Scalar degradation and (b)-(d)-(f) damage in tension. (a)-(b) Contour plots for a conical insert, (c)-(d) for a spherical/S13 insert, and (e)-(f) for a spherical insert/S16. The same contour scale applies to all plots.

3.2.4 Inserts interaction distance study

To optimise the efficiency of percussive drilling, it is necessary to place the inserts on the drill bit such that two consecutive impacts (in time) of the same bit give the largest removed volume. Experimental tests have been reported by Aldannawy [12] where two consecutive impacts with one insert have been performed where the distance between the impacts has been varied.

The above-mentioned described tests, i.e., two consecutive impacts with the same insert, are then simulated using the calibrated model. The same model as the one described in the previous sections has been used where one insert with the same shape has been added, see Figure 12. The impact bar on the left, grey colour, which is the one providing the first impact, is fixed, while the second impact bar, red colour, is placed at 0.5, 5.5, 7.5, 10.5, 12.5, 15.5 and 17.5 mm from the former. The simulations were run for two different insert shapes, the conical one, and a spherical one, so-called S13, as used in the previous section. A confining pressure of 30 MPa and an impact energy of 60 J were used.

The removed volume versus interaction distance from both experiments and modelling are shown in Figure 13. The modelling shows the same trends as in the experiments, i.e., a higher volume is removed with conical inserts than with spherical/S13 ones. The maximum removed volume for the conical inserts is obtained for the same interaction distance as in the experiments, i.e., about 7.5 mm; however, a lower interaction distance than in the experiments is obtained for the spherical inserts. Generally, for both insert geometries, the amount of removed volume is higher in the experiments than in the modelling.

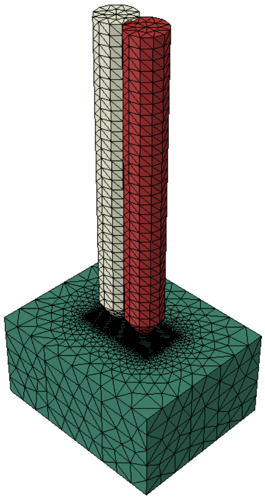

Figure 12: Mesh of the whole model for two consecutive impacts.

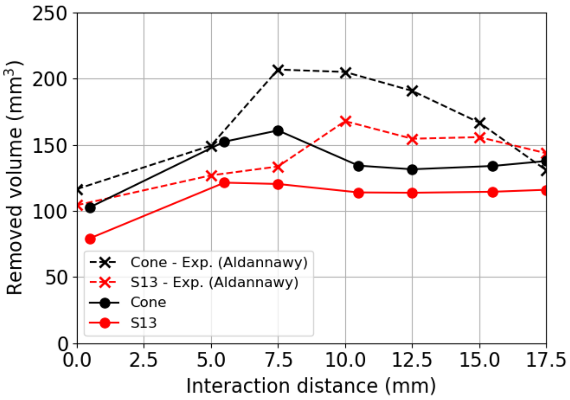

Figure 13: Removed volume versus interaction distance from experiments [12] (dashed lines) and modelling (solid lines).

4 Drill bit-rock interaction

In the following, the focus is set on the interaction between the full drill bit and the rock. The drill bit considered here is the one designed early 2022 in WP4 of the ORCHYD project, see Figure 14. It has 4 spherical inserts and 12 conical inserts. Conical inserts, although with a slightly different geometry than the one used in the dynamic indentation tests, have been chosen for their proven better efficiency with respect to rock removal [12]. The position between the inserts was chosen based on the tests results from Aldannawy [12]. Finally, semi-spherical inserts were placed at the outer periphery.

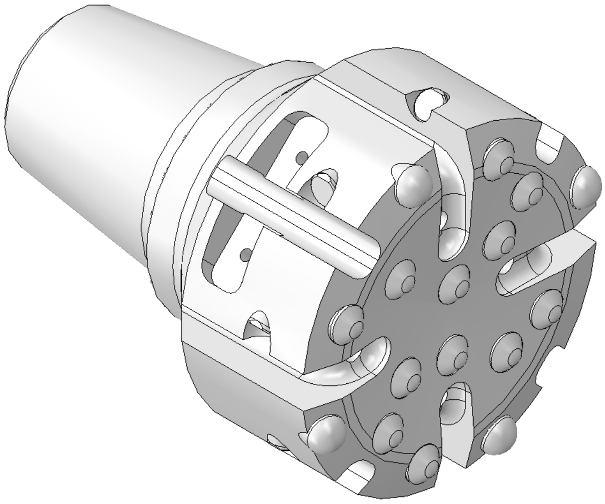

Figure 14: Hammer used as basis for the position of the inserts, considered in the current report.

4.1 Drill bit inserts shape

The effect of the shape of the inserts, is investigated here to justify the choice of a drill bit with inserts having different shapes. A simulation was run with a drill bit where all 16 inserts had a semi-spherical shape and compared to the reference case having 4 spherical inserts and 12 conical inserts, see Figure 15. The drill bit with 16 semi-spherical inserts was built by simply replacing the inserts in the reference case, i.e., the position of the inserts was identical to the reference case. A flat bottom hole geometry with a 10 mm deep groove was used.

In all simulations an energy impact of 995 J was used, i.e., about 62 J per insert: the inserts were given a total mass of 21.6 kg and an initial velocity of 9.6 m/s; only the inserts from the drill bit were modelled. A constant weight-on-bit of 15 kN was applied on the inserts. The rock volume modelled was cylindrical in shape with an external diameter of 300 mm and a height of 300 mm. Figure 16(a) shows the finite element model. The depth of the drilling hole, from the upper plane to the top (for flat, concave, and parabolic profiles) or bottom (for the pure parabolic profile) of the profile, i.e., measured along the model's axis, was 100 mm. The objective is to simulate drilling at a depth of about 4-5 km[1]. A constant pressure of 100 MPa was set on the external horizontal and vertical walls – σ_H and σ_V in Figure 16(b) – while a constant pressure on the bottom-hole, inner walls and groove walls was set to 40 MPa – σ_M in Figure 16(b). A stress of 100 MPa was initially set to the whole rock volume – σ_{rock} in Figure 16(b). The bottom face of the volume was fully constrained, and the inserts were constrained to move only vertically. The explicit solver of Abaqus was used.

The inserts were modelled as rigid bodies and meshed with 17,417 and 21,375 rigid elements, R3D4 and R3D3, for the bit with both spherical and conical inserts, and only spherical inserts, respectively. The rock was discretized with between about 683,058 quadratic tetrahedral elements, C3D10M, for both cases. The tetrahedral elements in the impact area on the rock had an edge length of about 3 mm. A clearance of less than 1×10^{-5} mm was set initially between the insert tips and the rock to avoid initial penetration. Note that due to the mesh discretization, all insert tips were not likely to be exactly at the same position.

Because the inserts are all rigid and can only displace in the vertical direction with the same velocity time history, it is as if the mass of each insert, when combined, carries the total mass

---

[1] Geostatic pressure is about 22 MPa per kilometre.

of the bit but moves as one joined rigid body. It is a valid representation of the full bit with embedded inserts which greatly simplifies the simulation. Using the initial impact velocity and bit mass as the initial conditions, the force and penetration with time after impact are the emergent behaviours together with internal rock damage and broken out fragment volume that is simulated with Abaqus.

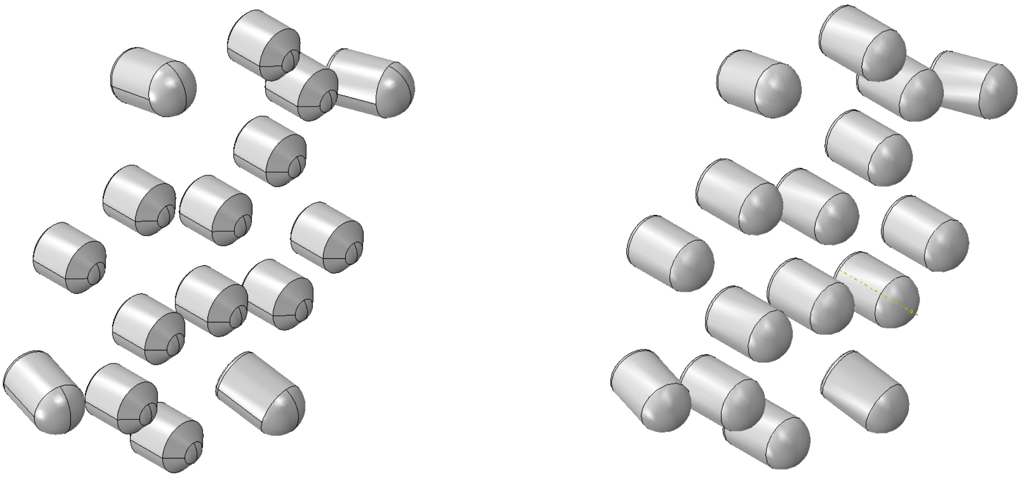
(a) (b)

Figure 15: Drill bit with (a) 4 spherical and 12 conical inserts and (b) 16 spherical inserts.

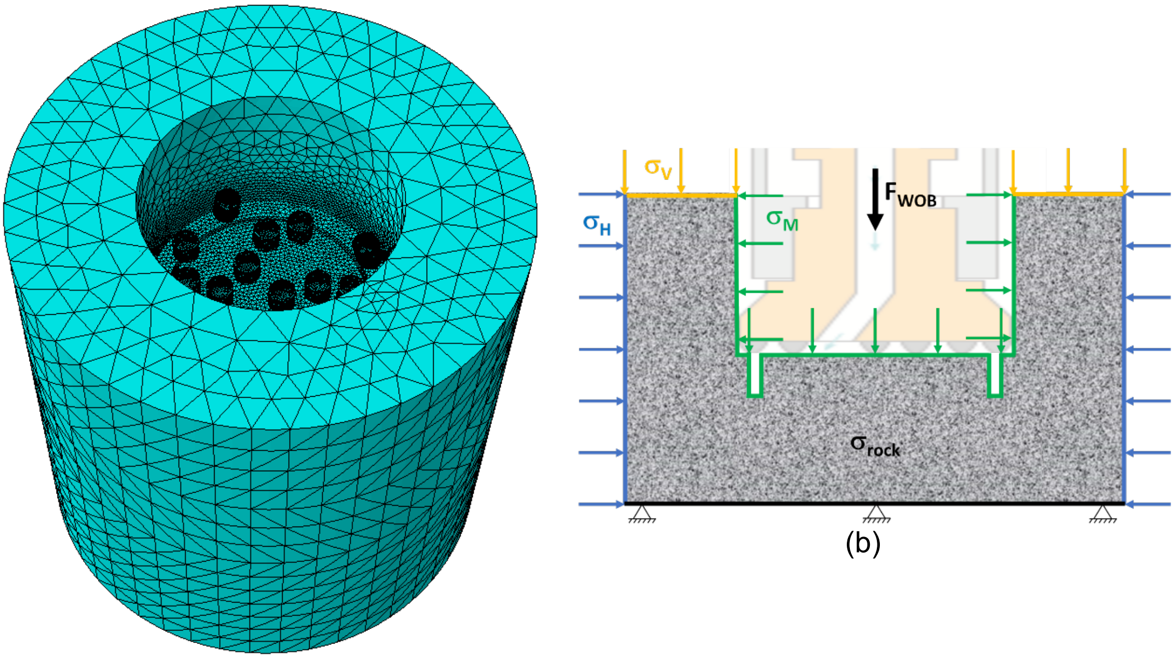

(a) (b)

Figure 16: Example of full finite element model.

Figure 17(a) and (b) show the force versus penetration curves and volume removed, respectively. The force shown is the normal force due to contact pressure at the insert-rock interface while the displacement is taken at a reference node on the bit – it is reminded that the bit is modelled as rigid. Using a drill bit with only spherical inserts gives a higher impact load and lower penetration than having a mix of conical and spherical inserts. Likewise, an about 55% lower removed volume is obtained when using a drill bit made of only spherical inserts.

Figure 18(a) and (b) show the accumulated damage for both types of drill bits with a threshold of 0.85. The contour plots are very similar to each other, but a somewhat lower damage is observed just underneath the inserts for nine of them, when those are spherical, which is not observed when they are conical. Those nine inserts have their axis normal to the rock surface. An area with lower damage at the centre of the indents is observed for the spherical inserts. This related most likely to how the contact pressure is distributed. It might be concluded that, for the chosen interaction distance, having a combination of different insert geometries is more efficient than having only spherical ones. However, it should be noted that the optimum interaction distance depends probably on the insert geometry.

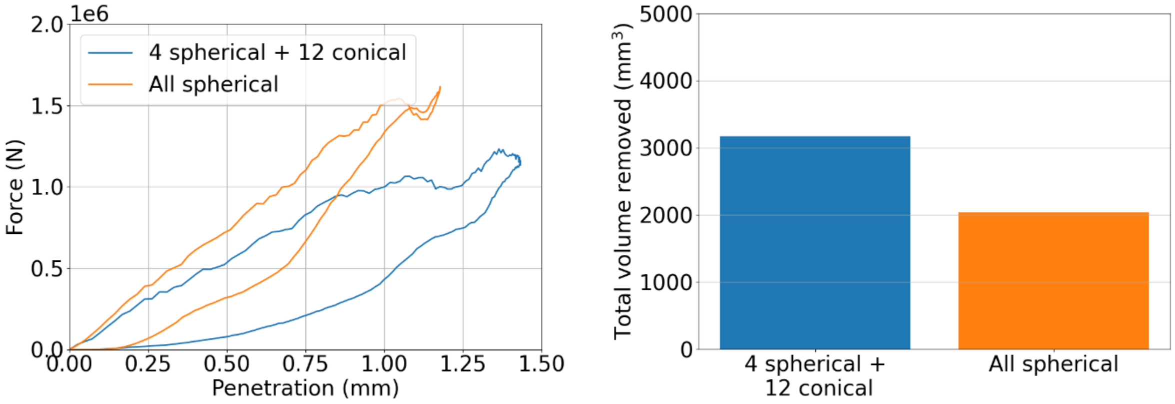

(a) (b)

Figure 17: (a) Force versus penetration curves and (b) volume removed, for different drill bit designs.

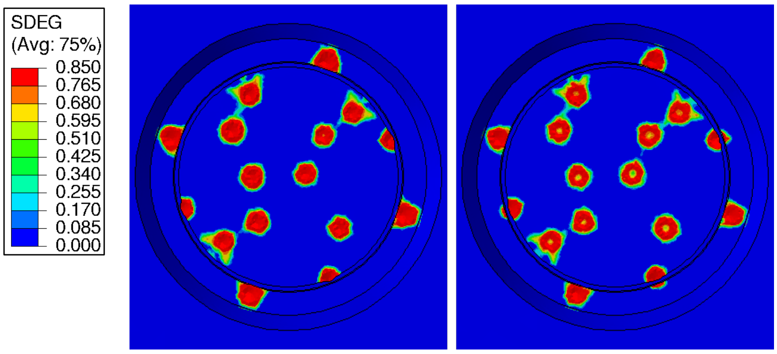

(a) (b)

Figure 18: Contour plots of accumulated damage for a drill bit with (a) 4 spherical and 12 conical inserts, and (b) 16 spherical inserts.

4.2 Effect of bottom hole geometry

Simulations of one impact of a 6" drill bit against the Red Bohus granite under downhole conditions were performed using the calibrated model. The drill bit was made of 16 inserts, among which 12 had a conical shape and 4 a spherical shape; only the inserts from the drill bit were modelled. Four different profile geometries were considered: flat, concave, parabolic and pure parabolic, see Figure 19. The effect of a groove, supposedly generated by a high-pressure water jet, was also investigated: no groove, 10 mm and 30 mm deep. The groove was 3 mm wide and had a mean diameter of 124 mm. There were altogether twelve different configurations investigated. The groove is formed by a high-pressure water jet placed on the drill bit. The study is supposed to take place under steady state conditions where the groove is already formed.

The inserts were modelled as rigid bodies and meshed with about 22,600 rigid elements, R3D4 and R3D3, see Figure 20(a). The rock was discretized with, depending on the profile geometry, between about 414,000 and 565,000 quadratic tetrahedral elements, C3D10M, Figure 20(b). The tetrahedral elements in the impact area on the rock had an edge length of about 3 mm. In all simulations an energy impact of 995 J was used, i.e., about 62 J per insert: the inserts were given a total mass of 21.6 kg and an initial velocity of 9.6 m/s. A constant weight-on-bit of 15 kN was applied on the inserts. The rock volume modelled was cylindrical in shape with an external diameter of 300 mm and a height of 300 mm. The depth of the drilling hole, from the upper plane to the top (for flat, concave, and parabolic profiles) or bottom (for the pure parabolic profile) of the profile, i.e., measured along the model's axis, was 100 mm. A constant pressure of 100 MPa was set on the external horizontal and vertical walls while a constant pressure on the bottom-hole, inner walls and groove walls was set to 40 MPa. An internal stress of 100 MPa was initially set to the rock (this corresponds to a drilling depth of about 4-5 km). The bottom face of the volume was fully constrained, and the inserts were constrained to move only vertically. The explicit solver of Abaqus was used to solve this problem.

Note that the simulations take typically about one hour to run on a Linux workstation when using 4 Intel Xeon 6136 processors.

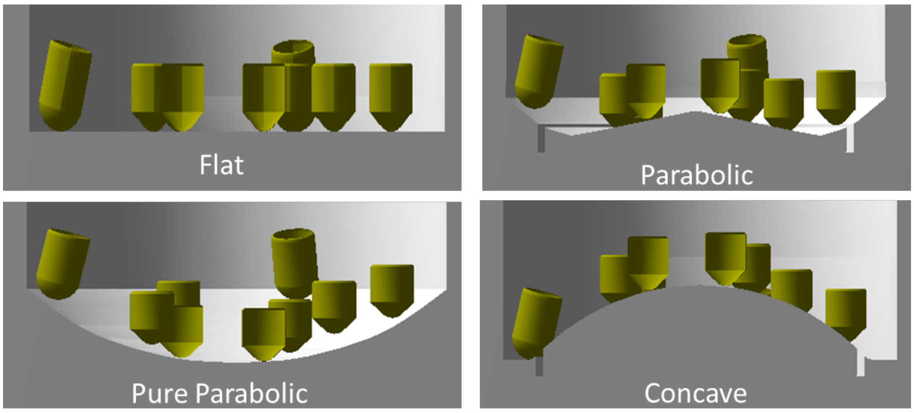

Figure 19: The four profile geometries investigated with examples of grooves.

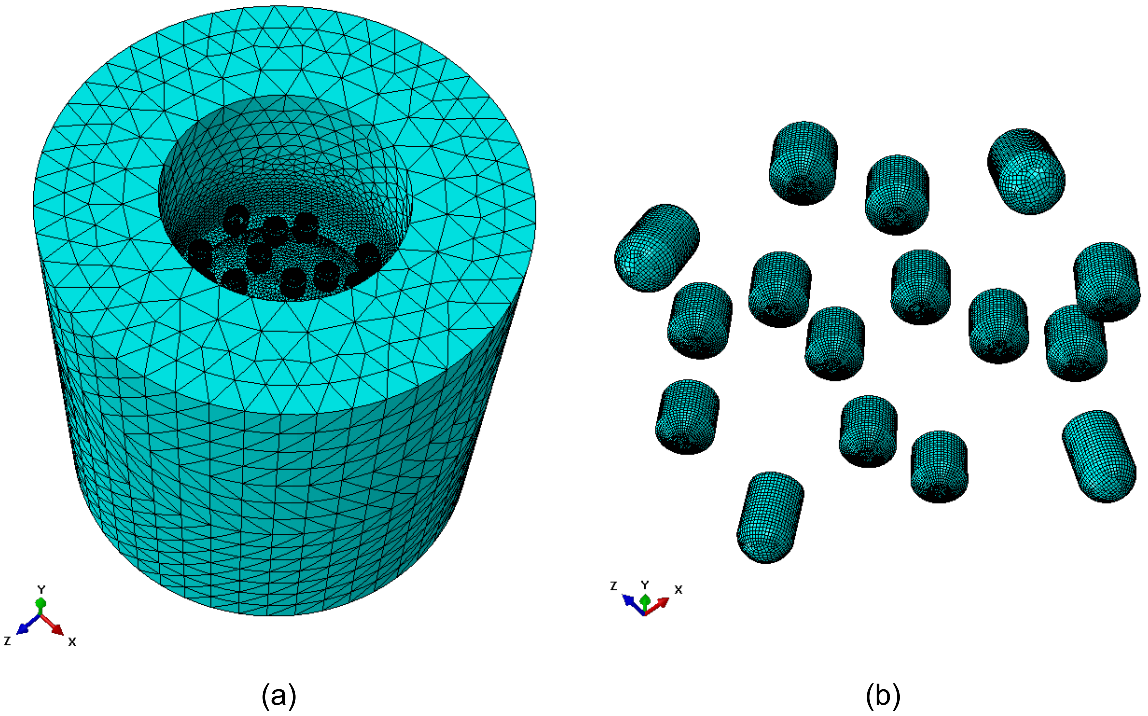

Figure 20: (a) Example of full finite element model, (b) finite element mesh for the inserts.

Figure 21 shows the force versus penetration curves for each profile and groove depth. The force shown is the normal force due to contact pressure at the insert-rock interface while the displacement is taken at a reference node on the bit. The shape of the curves is affected by stress waves propagating in the medium. All configurations generate maximum impact loads from about 1000 to 1800 kN and maximum penetrations from 1.0 (flat profile without groove) to 1.5 (parabolic profile with groove depth of 30 mm) mm. Increasing the depth of the groove decreases the impact load and increases the maximum penetration at the same time. However, the effect of groove depth on penetration is the least for the concave profile. The largest decrease in impact load, due to having a groove versus no groove, is observed for the flat profile; the least decrease is seen for the concave profile. Similarly, the largest increase in maximum penetration due to the groove is observed for the flat profile and the least increase is seen for the concave profile. Finally, the permanent penetration, or indent depth, increases with the groove depth.

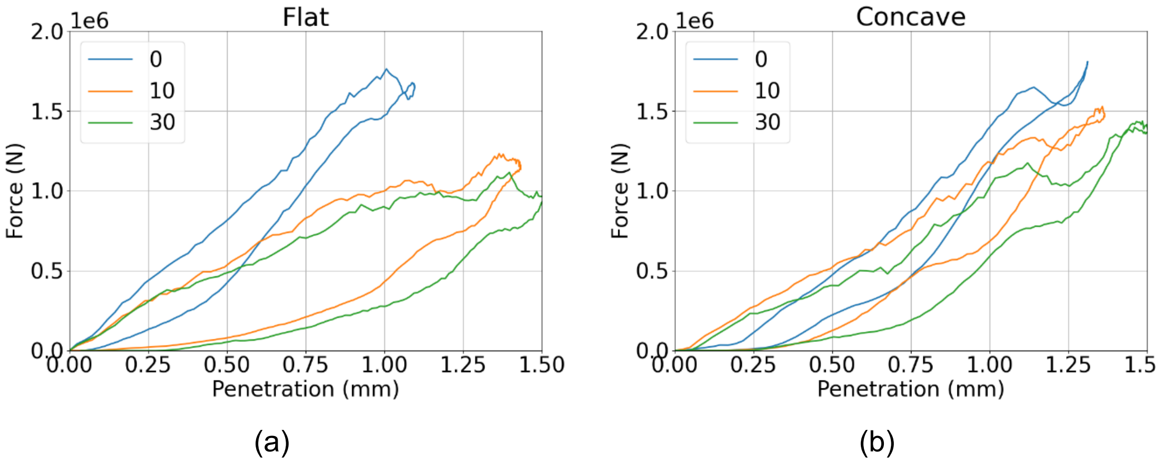

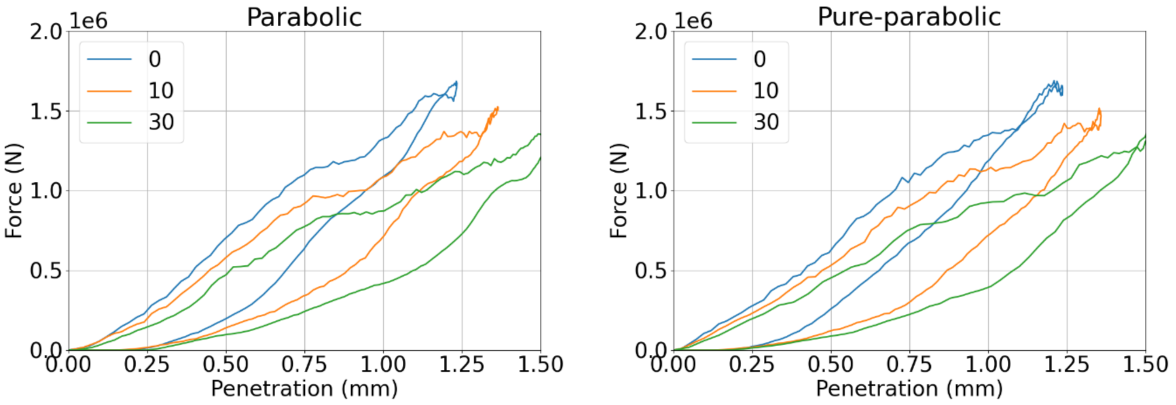

(c) (d)

Figure 21: Force versus penetration curves for (a) flat, (b) concave, (c) parabolic and (d) pure parabolic profile, for different groove depths (in mm).

Figure 22, Figure 23, Figure 24 and Figure 25 show contour plots for flat, concave, parabolic and pure-parabolic profiles, respectively, at the end of the unloading; the cut-off for the damage in the plots is 0.85, i.e., damage, or scalar degradation (Eq. (7)), higher than 0.85 is of the same colour, red. Sub-figures (a), (b) and (c) show the rock from above, along the model's axis, to show the whole area of impact; sub-figures (d), (e) and (f) show the rock from a different viewpoint with cuts to show how damage is distributed within the bulk. At first, we focus on the effect of the groove on the distribution of damage around and especially between indents. These figures show that increasing the groove depth increases the damage below, around and between indents. It can be seen that even without any groove, there is more damage between indents for the concave profile than for the other profiles. When the groove is 10 mm deep, the highest damage between indents is observed for the concave profile and, to a lesser extent, the flat and parabolic profiles; no noticeable damage is observed between the indents for the pure-parabolic profile. However, when the groove is 30 mm deep, damage between the indents is increased for all profiles but is largest for the flat and parabolic profiles. As observed in sub-figures (g), (h) and (i), the tensile damage around and between the indents is higher with a groove than with none, whatever the profile geometry. This is attributed to a stress release effect induced by the groove. Furthermore, the deeper the groove the larger the stress release. It is worth noting that the occurrence of damage between indents would promotes chipping; therefore, the higher and the deeper this damage, the larger would chipping be. Although the scalar degradation between the inserts is below 0.85, it might be that the critical damage in tension itself is actually lower.

We focus now on the interaction between groove and inserts located near the groove. The figures show that the extent of damage higher than 0.85 (red spots) in the central zone of the rock, i.e., away from the groove, is little affected by the presence of the groove. However, in the periphery zone, i.e., near the groove, there is an increase of damage and extent of damage (size and volume of the red spots) of the indents near the groove (compare figures (a) and (b) with (c)); this is particularly seen for the flat, parabolic, and concave profiles. This is again believed to be due to the stress release effect mentioned above.

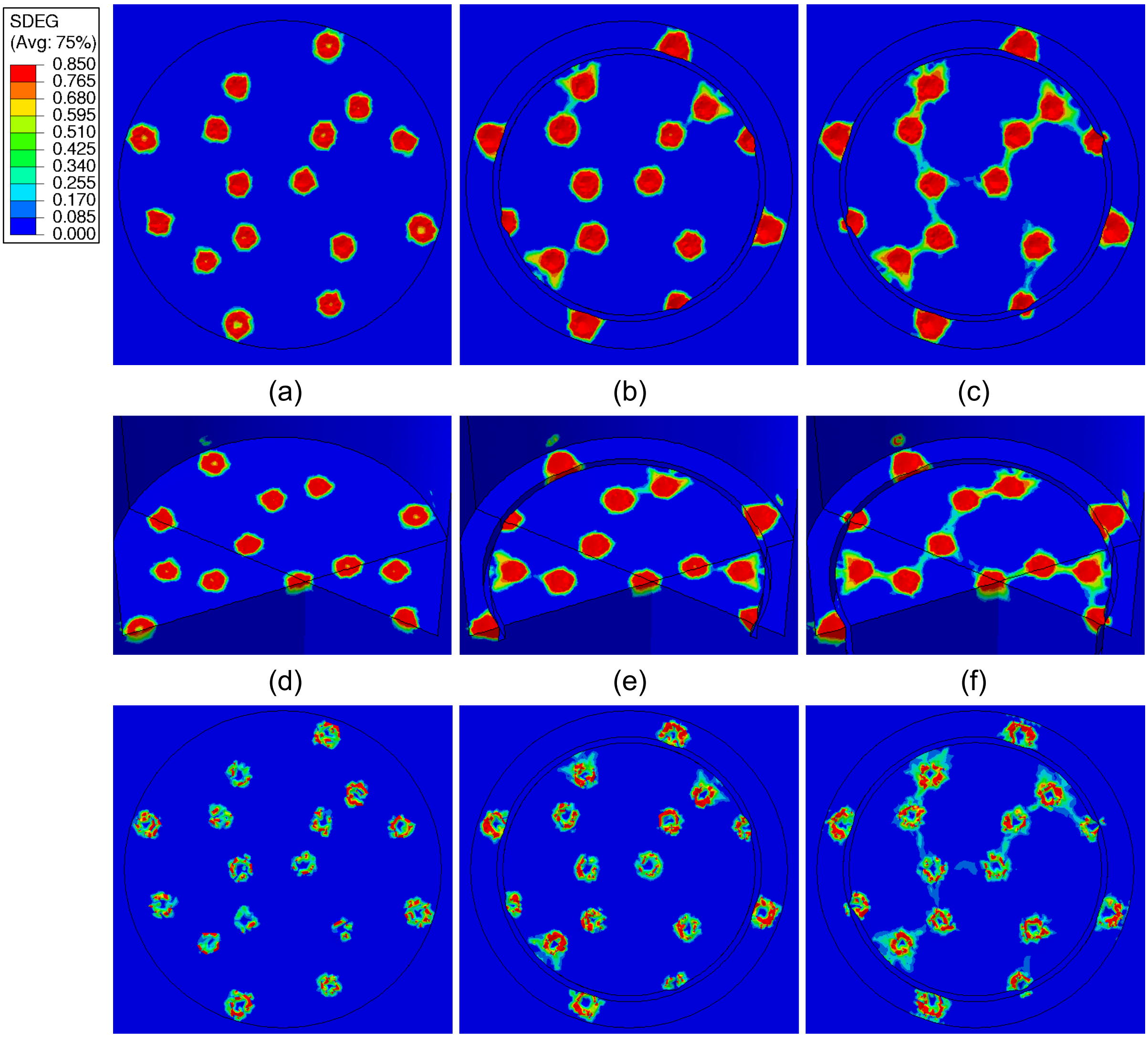

(a) (b) (c)

(d) (e) (f)

(g) (h) (i)

Figure 22: Contour plots of accumulated damage for flat profile with (a)(d)(g) 0, (b)(e)(h) 10 and (c)(f)(i) 30 mm deep groove. (a), (b) and (c) seen from above along model's axis, (d), (e) and (f) seen from a different viewpoint with cuts. (a) to (f) show the scalar degradation variable while (g), (h) and (i) show the tensile damage variable.

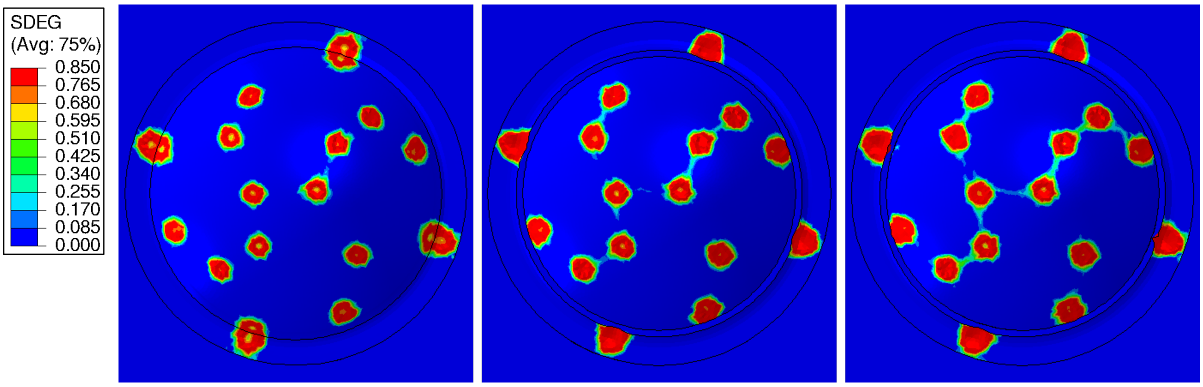

(a) (b) (c)

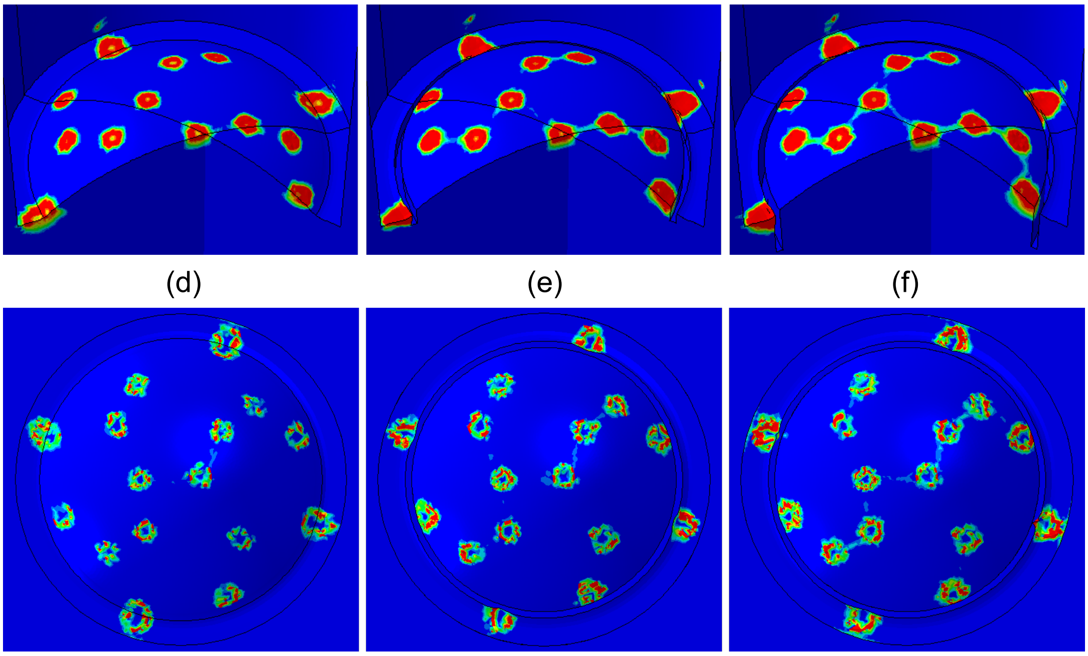
(d) (e) (f)

(g) (h) (i)

Figure 23: Contour plots of accumulated damage for concave profile with (a)(d)(g) 0, (b)(e)(h) 10 and (c)(f)(i) 30 mm deep groove. (a), (b) and (c) seen from above along model's axis, (d), (e) and (f) seen from a different viewpoint with cuts. (a) to (f) show the scalar degradation variable while (g), (h) and (i) show the tensile damage variable.

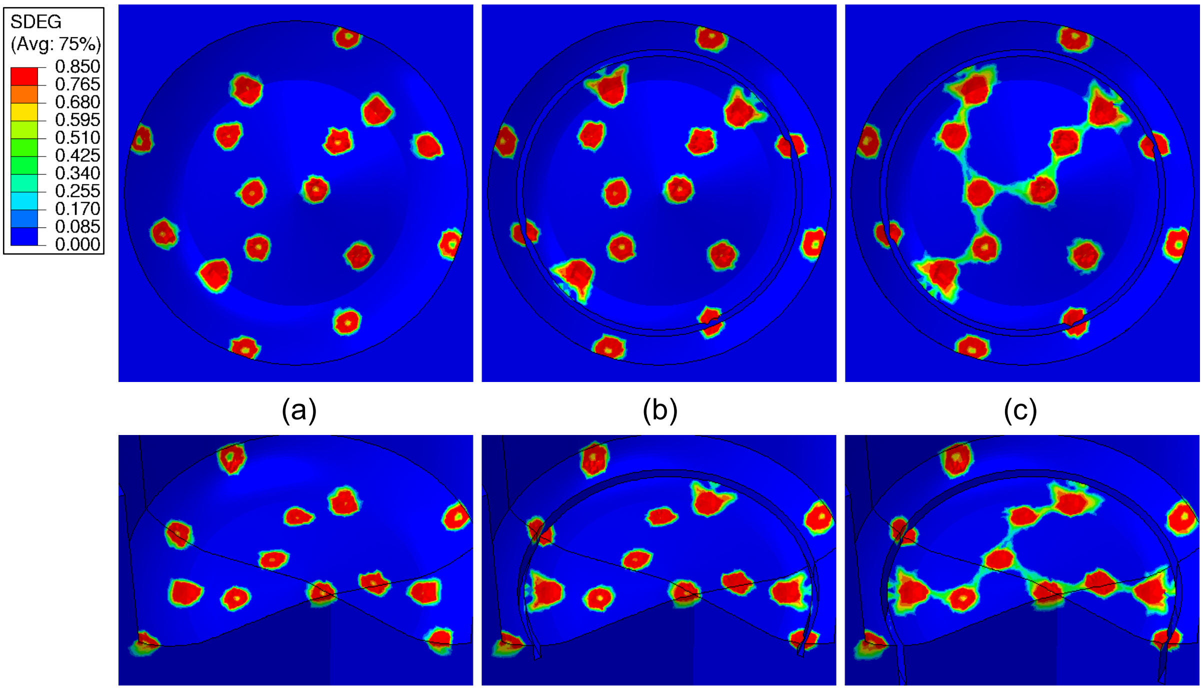

(a) (b) (c)

(d) (e) (f)

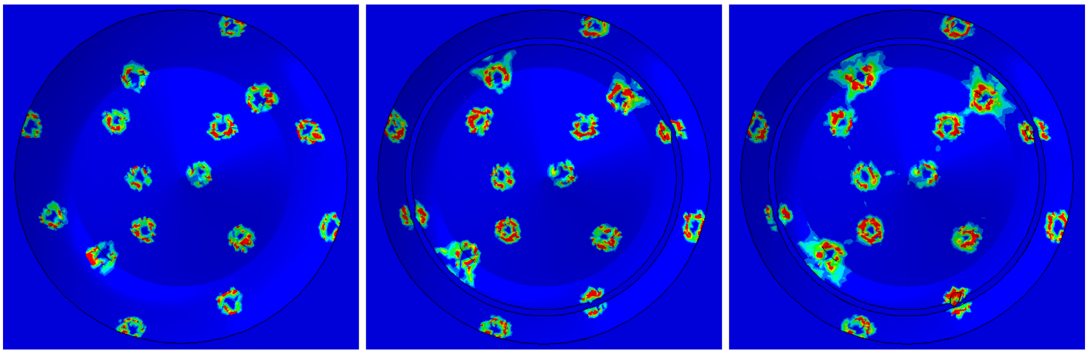

(g) (h) (i)

Figure 24: Contour plots of accumulated damage for parabolic profile with (a)(d)(g) 0, (b)(e)(h) 10 and (c)(f)(i) 30 mm deep groove. (a), (b) and (c) seen from above along model's axis, (d), (e) and (f) seen from a different viewpoint with cuts. (a) to (f) show the scalar degradation variable while (g), (h) and (i) show the tensile damage variable.

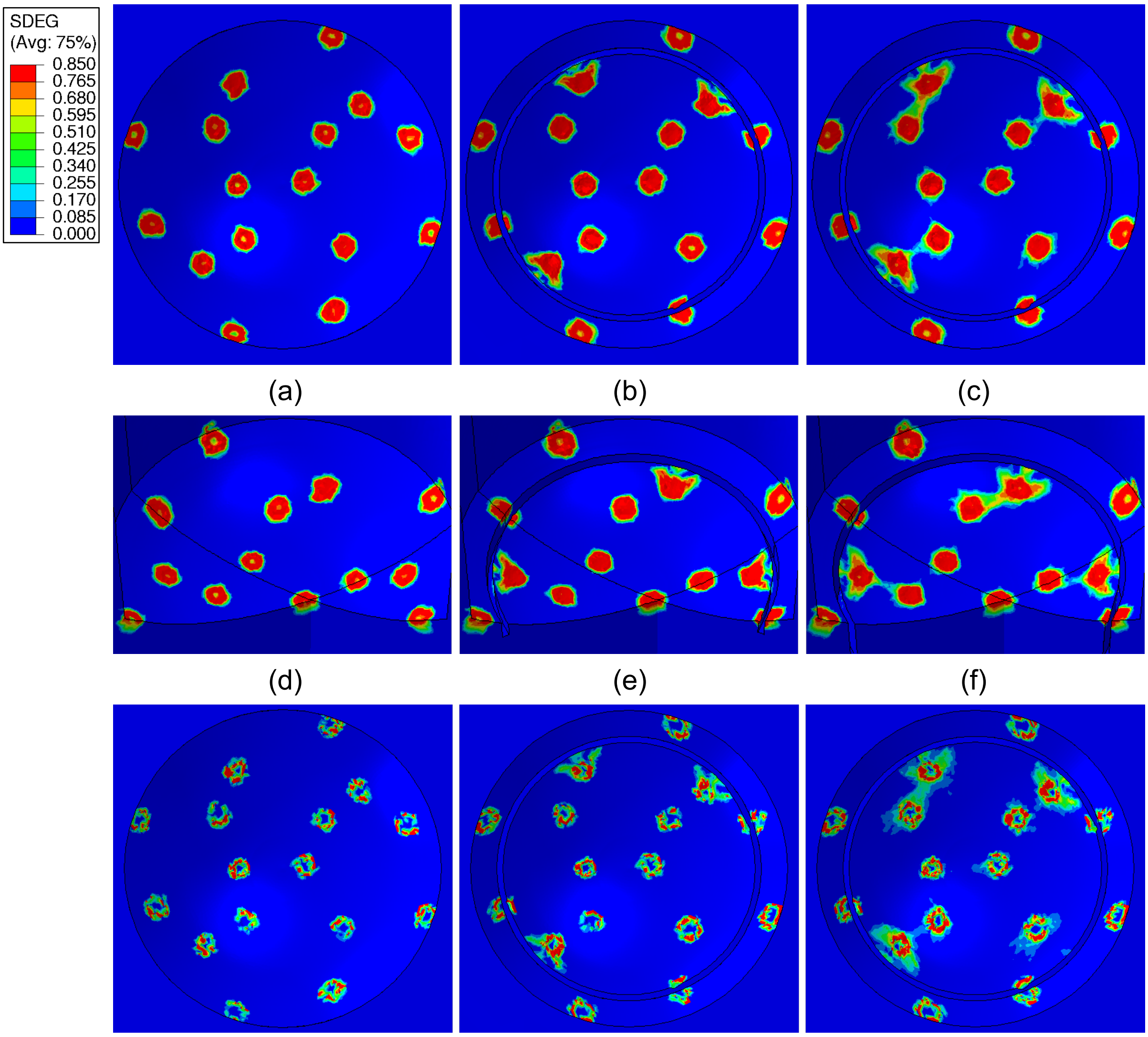

(a) (b) (c)

(d) (e) (f)

(g) (h) (i)

Figure 25: Contour plots of accumulated damage for pure-parabolic profile with (a)(d)(g) 0, (b)(e)(h) 10 and (c)(f)(i) 30 mm deep groove. (a), (b) and (c) seen from above along model's axis, (d), (e) and (f) seen from a different viewpoint with cuts. (a) to (f) show the scalar degradation variable while (g), (h) and (i) show the tensile damage variable.

The above observations indicate that the volume of rock fractured or removed increases with the depth of the groove, and that rock fracture would be larger at the periphery zone than the central zone. Therefore, the volume fractured or removed, defined as the volume of elements which for the damage is higher than the critical damage d_{crit} of 0.85, has been computed for each configuration. Note that C3D10M elements have 4 integration points; an element is considered as fractured if at least one integration point reaches a damage higher than the critical damage.

Figure 26(a) shows the total volume removed, i.e., for all elements in the rock fulfilling $d_{crit} \geq 0.85$. It clearly appears that increasing the groove depth increases the volume removed as suggested previously. It can also be seen that there is a strong effect of the shape of the profile, where the flat and concave profiles produce the largest volume removed when a groove is present. However, both profile and groove depth have a limited effect for the parabolic-type profiles.

The flat profile gives the largest removed volume when grooves are introduced, by more than 3 times with a groove depth of 10 mm, but is much less increased when increased to 30 mm. This contrast with the findings of WP4 on stress release, where it was suggested that the effect only really kicks in for a groove depth of 10 mm and is much better with a depth of about 20-30 mm.

Larger volume removed would be expected for higher penetration. This is however not always true, compare Figure 21 with Figure 26(a), as well as observed experimentally by Aldannawy [12]. With the constitutive model used here, penetration in Figure 21 relates to both plasticity and damage while volume removed relates only to damage higher than 0.85. Figure 26(b) shows the area enclosed in the force versus penetration curves from Figure 21. A similarity appears with the volume removed when comparing flat profile with parabolic profiles but not for the concave profile which has the lowest area for all groove depths. Again, with the model used here, the area enclosed in the force versus penetration curve encompasses both plasticity and damage while volume removed relates only to damage higher than 0.85.

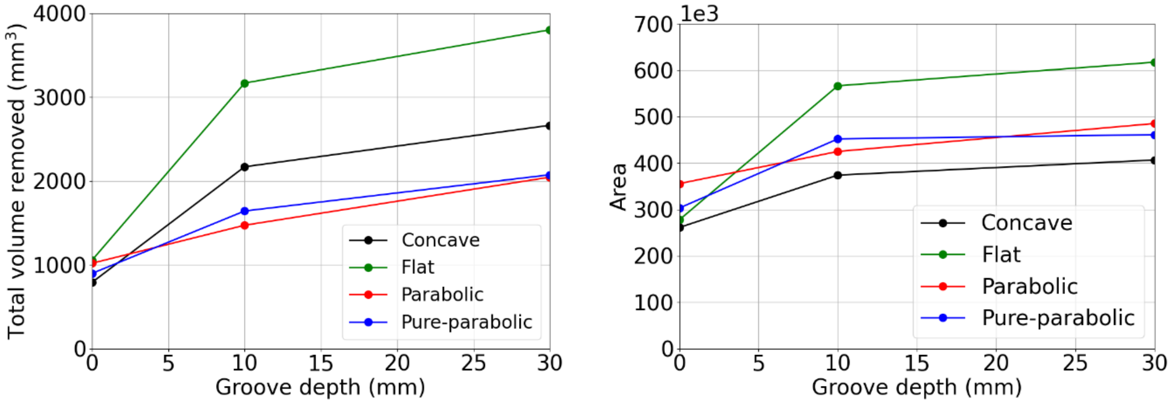

(a) (b)

Figure 26: (a) Total volume removed and (b) area enclosed in force versus penetration curves from Figure 21, for each profile and for different groove depths.

Next the effect of the position of the inserts, with respect to the groove, on the volume removed is investigated. The numbering of the inserts on the drill bit is shown in Figure 27. Six inserts – set 1, insert number 3, 4, 6, 7, 8 and 12, black in Figure 27 – are located between 10 and

40 mm from the axis, or centre, of the drill bit. They are not in contact with the groove at all, whatever the profile geometry, although they somehow interact with it since there is a stress release effect. Three inserts – set 2, insert number 2, 9 and 10, green in Figure 27 – are located 50 mm from the centre and are closer to the groove. The three next – set 3, insert number 1, 5 and 11, blue in Figure 27 – are located 60 mm from the centre and are yet closer to the groove. The remainder four inserts – set 4, insert number 13, 14, 15 and 16, red in Figure 27 – with spherical shape, are located on the outer periphery of the drill bit, 70 mm. Depending on the profile geometry, set 1, 2 or 3 interact with the groove see Figure 22, Figure 23, Figure 24 and Figure 25. The volume removed under each insert, i.e., for elements in the rock fulfilling $d_{crit} \geq 0.85$, is computed and summed up for each set. The proportion of volume removed for each set is then computed and shown in Figure 28.

At first, it should be noted that, generally, the proportion of volume removed at the different locations, i.e., related to the position of the different sets of inserts, changes notably when a groove is introduced. The presence of a groove decreases the proportion of volume removed by inserts in set 1, i.e., those closest to the centre of the drill bit, with the strongest effect on flat and concave profiles, but least on the parabolic profile. The volume removed amounts to 20 to 40% depending on the profile geometry. The trend for set 2 is the same for flat and concave profiles, i.e., the presence of the groove leads to lower volume removed, while the groove has a positive effect for the parabolic and pure-parabolic profiles. The volume removed amounts to 10 to 20% for the former and 20 to 40% for the latter. For set 3, which interacts directly with the groove for all profile geometries, the presence of the groove has little to no effect on the volume removed, which amount to about 10 to 20%. However, for set 4, the groove has no effect on the volume removed for the parabolic and pure-parabolic profiles but has a strong effect for the flat and concave profiles. For the flat and concave profiles, about 40 to 60% of the total volume removed is attributed to those inserts when there is a groove. In conclusion, when a groove is present, most of the volume removed is attributed to the inserts located at the outer periphery, set 4, for the flat and concave profiles, while for the parabolic and pure-parabolic profiles, most of the volume removed is attributed to the inserts located closer to the centre, i.e., sets 1 and 2. However, it is worth noting because the groove is modelled with perfect rectangular geometry and a real groove would be V-like, the difference in volume removed between no groove and 10 mm groove related to set 4 may be overestimated.

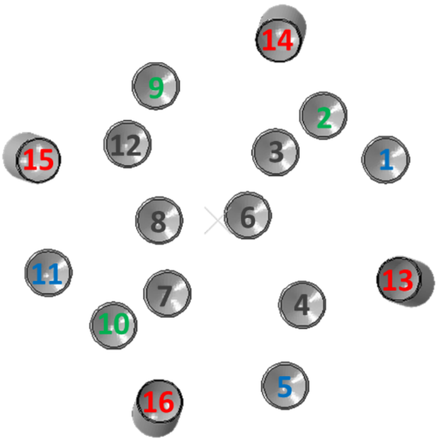

Figure 27: Numbering of the inserts on the drill bit. A colour is attributed to each set to distinguish them from each other.

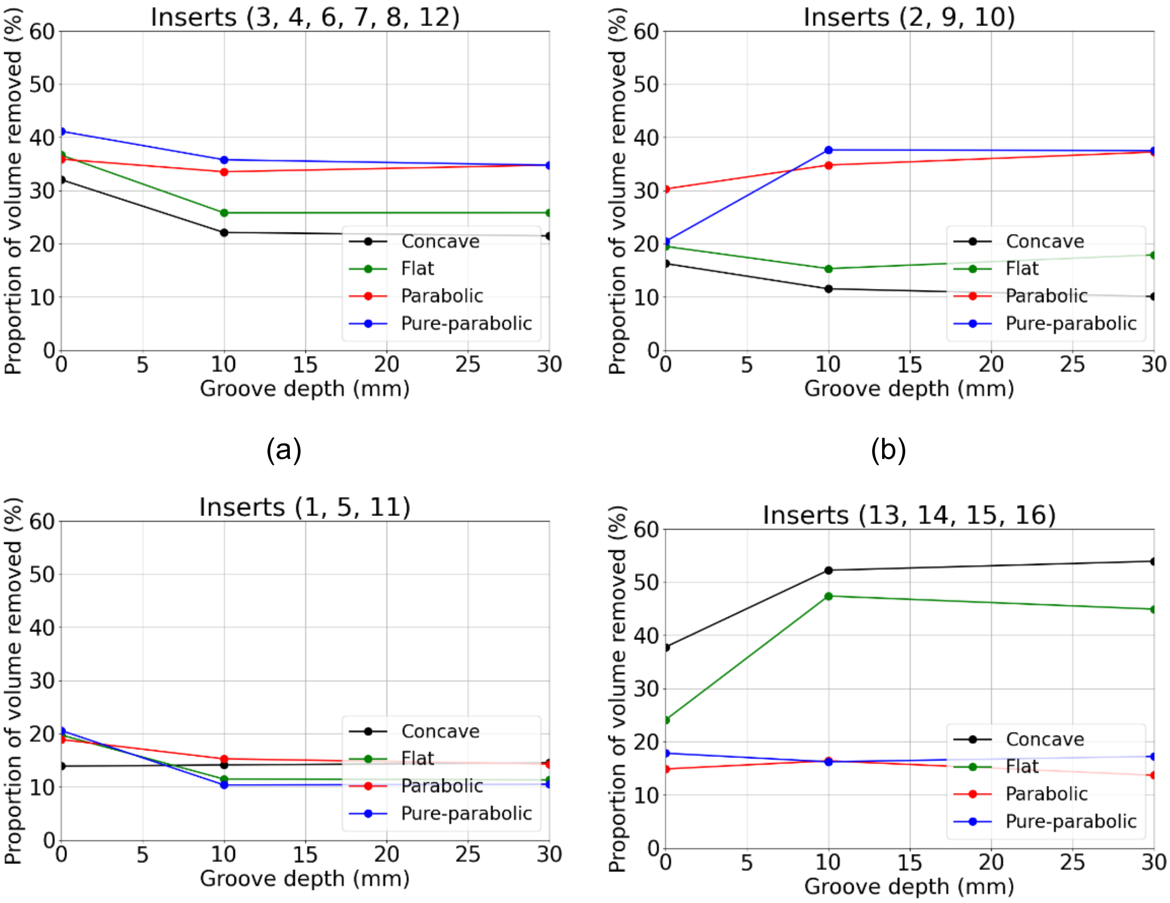

(a) (b)

(c) (d)

Figure 28: Volume removed by each set of inserts, for each profile and for different groove depths.

4.3 Simulation loading hypotheses

The stress release effect we are considering here (induced by the groove created with high-pressure water jet), is the potential influence of the release of the high internal stresses present in the rock in order to ease the rock removal during percussive rotary drilling. The process of creating a groove is a continuous process where the water jet impacts the rock while the drill bit rotates. Stress release thus occurs locally while the water jet impacts the rock. Geometrically speaking, the groove is created before impact. However, timewise, stress release occurs while the water jet impacts the rock. In order to assess the effect of stress release, two modelling approaches are considered: i) a simultaneous one and ii) a sequential one. What happens in reality lies most likely somewhere between these two approaches.

In the simultaneous approach, the simulation was performed in one step, i.e., the same procedure as above, Section 4.2, is followed: a constant pressure of 100 MPa was set on the external horizontal and vertical walls, a constant pressure of 40 MPa was set on the bottom-hole, inner walls and groove walls, an internal stress of 100 MPa was initially set to the rock, while a weight-on-bit of 15 kN was applied and the rock was impacted at a velocity of 9.6 m/s. All those boundary conditions were applied simultaneously using the explicit solver of Abaqus.

In the sequential approach, the simulation was done in several steps. At first, there was no groove present in the rock; the rock was loaded statically where a constant pressure of 100 MPa was set on the external horizontal and vertical walls, a constant pressure of 40 MPa was set on the bottom-hole and inner walls, and an internal stress of 100 MPa was initially set to the rock. After equilibrium was reached, the groove was formed at once and a constant pressure of 40 MPa was set on the groove walls. These two steps were performed using the implicit solver of Abaqus. Then an explicit step was performed where the weight-on-bit, 15 kN, was applied and the rock was impacted, at a velocity of 9.6 m/s, both simultaneously.

All simulations were run using a flat profile. The effect of the position of the groove was also assessed for the sequential approach where a groove with a mean diameter of 147 mm was used. In summary, four configurations were compared: an impact on a rock i) without any groove using a simultaneous approach (Sim. 0-0-5), ii) with a 10 mm deep and 124 mm mean diameter groove using a simultaneous approach (Sim. 10-124-5), iii) with a 10 mm deep and 124 mm mean diameter groove using a sequential approach (Seq. 10-124-5) and iv) with a 10 mm deep and 147 mm mean diameter groove using a sequential approach (Seq. 10-147-5). The effect of drilling depth was also assessed by running a simulation where the initial rock stress and external horizontal pressure were set to 200 MPa, corresponding to a drilling depth of about 10 km (Seq. 10-124-10).

The results of force versus penetration and volume of rock removed (for each simulation) are shown in Figure 29(a) and Figure 29(b), respectively.

Figure 29© shows the area enclosed in force versus penetration curves, or energy dissipation. In absence of groove, both the bit penetration and rock removed obtained with a simultaneous approach (blue data) are significantly reduced, from 2 to 3 times, compared with the results obtained with 10 mm deep groove, following the simultaneous approach (orange data) or the sequential approach (green, red, purple data).

Also, sequential approach results show than increasing the mean diameter of the groove or the drilling depth (red and purple data) brings the force versus penetration curve closer to that corresponding to a rock without groove, while the amount of rock removed, and dissipation, remain similar (within 15%). However, the position of the inserts with respect to the groove is not the same, i.e., the inserts are closer to the groove for a diameter of 124 mm, which may play an important role as shown in Section 4.2. This indicates that the direct interaction between groove and inserts seems to play a more important role than stress release.

Finally, changing the approach from simultaneous to sequential while assuming the same groove geometry and drilling depth (orange versus green data), revealed a small reduction of the bit penetration and a variation in volume removed and dissipation of about 15-20%. Note that in reality there is no groove with constant maximal depth all around. Furthermore, the groove is idealised; it has a V-like shape rather than a sharp U-shape, thus producing less stress concentrations. All those simulations probably overpredict the volume removed.

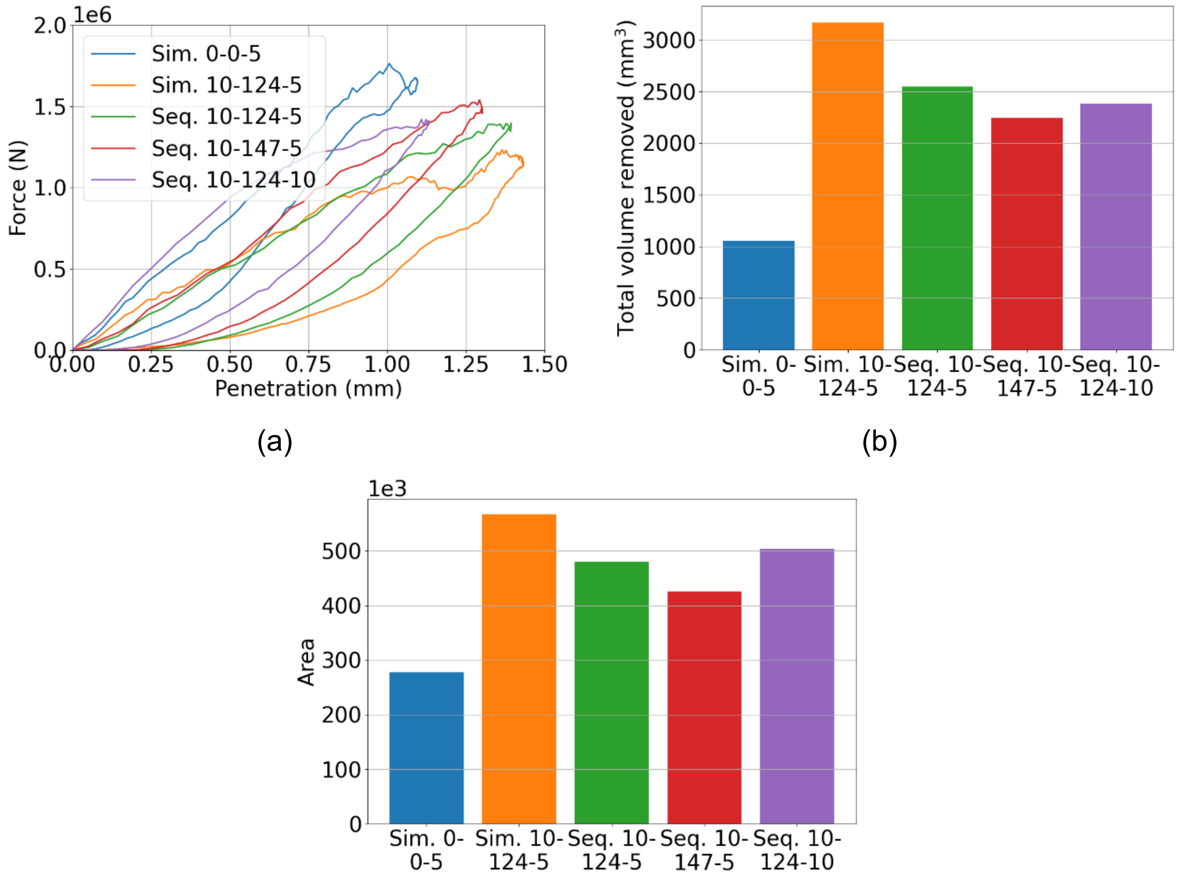

(a) (b)

(c)

Figure 29: (a) Force versus penetration, (b) volume removed and (c) area enclosed in force versus penetration curves in (a), for different modelling approaches and configurations.

4.4 Effect of drilling operating conditions

In this section, the effect of both impact energy and weight-on-bit is assessed. More simulations were run with impact energies of 40, 50 and 70 J per insert; this was achieved by changing the impact velocity to 7.7, 8.6 and 10.2 m/s, respectively. Two more simulations were run with a weight-on-bit of 20 and 25 kN, both for an impact energy of about 60 J per insert. All simulations were run using a flat profile and a groove depth of 10 mm.

Figure 30(a) and (b) show the force versus penetration curves for different impacts and weight-on-bits. Note that the green and blue curves in Figure 30(a) and (c), respectively, correspond to the reference case described in Section 4.2. While the weight-on-bit has no effect, both force and penetration increase with impact energy. The permanent penetration, penetration at 0 force, or indent depth, is affected by the impact energy, see Figure 30(b), with a ratio of about 2 when increasing the impact energy from 40-50 to 60-70 J.

Figure 31(a) and (b) show the volume removed for different impact energies and weight-on-bits, respectively. It clearly appears that the volume removed increases with the impact energy with an almost linear dependence as it increases by about 75% when the impact energy increases by 75%. However, there is no clear trend regarding the weight-on-bit as it does not affect the volume removed by more than about 3-4%. This correlates very well with the experimental observations done by Aldannawy et al. [12], see also Figure 8.

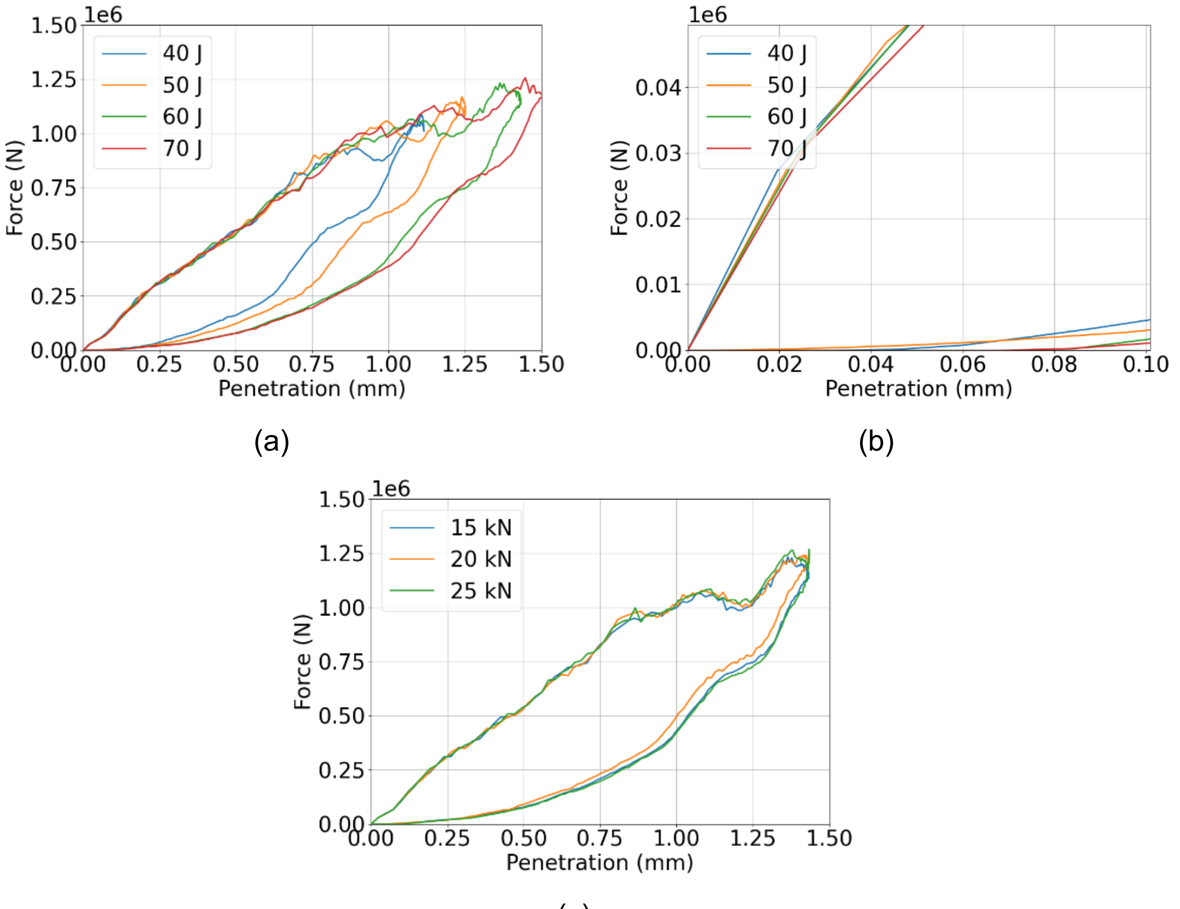

(a) (b)

(c)

Figure 30: Force versus penetration curves for different (a) impact energies per insert, (b) zoom-in on lower left corner of (a), and (c) weight-on-bits.

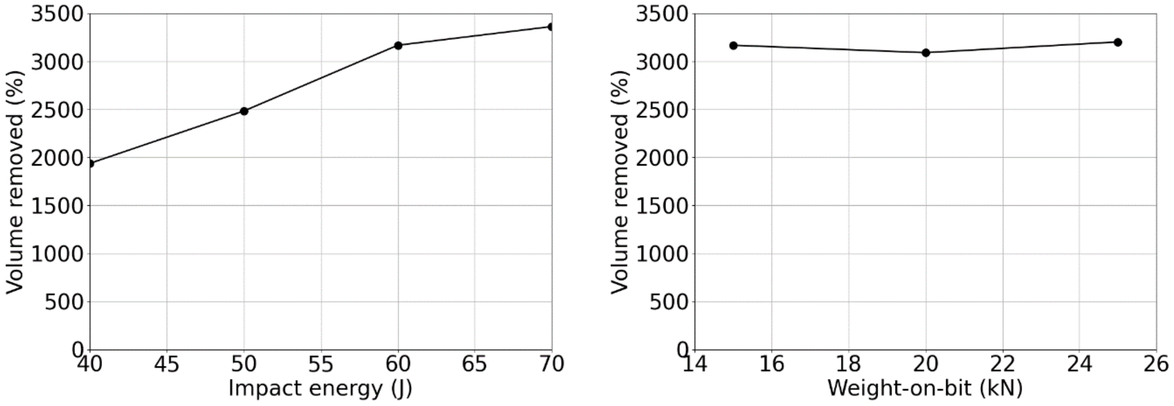

(a) (b)

Figure 31: Volume removed (mm^3) for different (a) impact energies and (b) weight-on-bits.

4.5 Effect of bottom hole geostatic conditions

The reference case is the simulation with a flat profile, a 10 mm deep groove and all other boundary conditions as stated in Section 4.2, i.e.: constant pressure of 100 MPa on external horizontal and vertical walls, constant pressure of 40 MPa on bottom-hole, inner walls and groove walls, initial internal stress of 100 MPa on the rock, corresponding to a depth of 4-5 km. Another simulation was run where the horizontal and vertical walls were subjected to a pressure of 20 MPa, the initial stress to the rock was set to 20 MPa, and the bottom-hole, inner walls and groove walls were subjected to a pressure of 10 MPa, which corresponds to a lower drilling depth of about 1 km. Weight-on-bit and impact velocity were unchanged.

Figure 32(a) and (b) show the force versus penetration curves and volume removed, respectively. As expected, the penetration is much higher at a lower depth, while requiring a lower force because of the lower geostatic pressure, and more than twice more volume is removed.

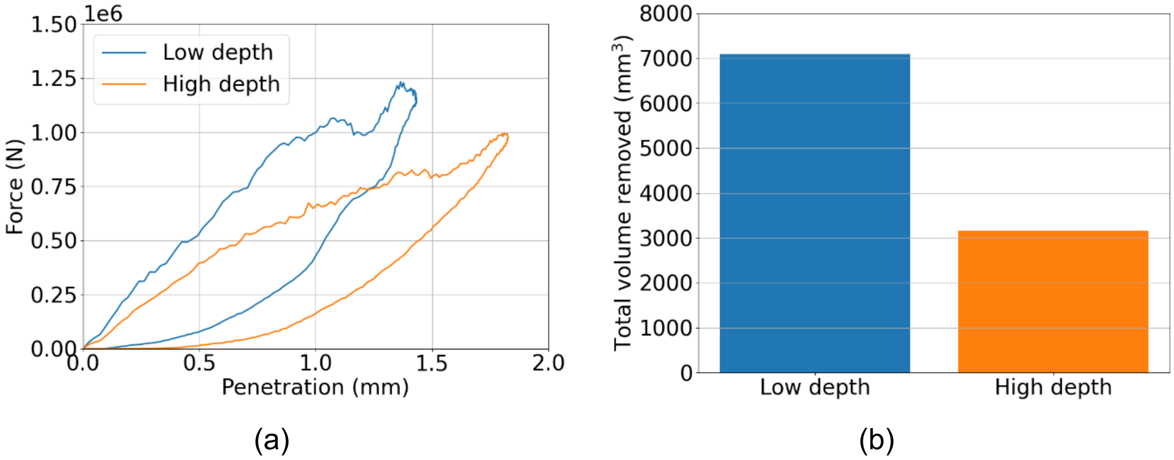

Figure 32: (a) Force versus penetration curves and (b) volume removed, for different bottom hole conditions.

4.6 Computational aspects

All simulations, except those for the single element calibration, were run on Linux workstations using 4 processors. Simulations with one and two inserts, Section 3.2.2.3 and 3.2.4, were run on a Linux workstation with Intel Xeon E5-2670 processors (2.5 GHz). All other simulations, Section 4, were run on a Linux workstation with Intel Xeon 6136 processors (3.0 GHz).

When using the explicit solver, domain-level parallelization and double precision were systematically used, with the mp_mode option consistently set to "threads".

All results shown in this report are extracted from the odb file using different Python scripts.

5 Conclusions

In this work, a continuum, isotropic elasto-visco-plastic, and damage-based model for concrete and other quasi-brittle materials, also called the concrete damaged plasticity (CDP) model, available in Abaqus, has been used, calibrated, and validated to study bit-rock interaction in rock percussive drilling. A study on the effect of insert geometry in single impact shows that a higher and deeper volume of rock is removed with a conical insert while a larger and deeper volume is damaged, but not necessarily removed, with spherical inserts. The volume removed due to damage in tension appears to be larger with the spherical inserts.

It is then shown that a drill bit with a combination of conical and spherical inserts is more efficient with respect to rock removal when compared to a drill bit made of only spherical inserts. The effect of bottom hole geometry, bottom hole conditions, drilling conditions and drill bit design have been assessed. The main conclusion from that study is that the presence of a groove with respect to rock removal is more beneficial than without groove. The study also shows that flat and concave geometries are the most efficient with respect to rock removal.

Impact energy has a strong influence on rock removal while weight-on-bit has little effect. Furthermore, the effect of drilling depth shows, as expected, lower rock removal for higher depths, due to higher confining pressure.

References

[1] M. Fourmeau, A. Depouhon, A. Kane, H.N. Hoang, F. Detournay, "Influence of indexation and impact energy on bit/rock interface law in percussive drilling: an experimental study", 49th U.S. Rock Mechanics/Geomechanics Symp. San Francisco, California, USA, 2015

[2] M. Fourmeau, A. Kane, M. Hokka, "Experimental and numerical study of drill bit drop tests on Kuru granite", Philosophical Transactions of the Royal Society A, vol. 375, 20160176, 2017, https://doi.org/10.1098/rsta.2016.0176

[3] M. Saadati, P. Forquin, K. Weddfelt, P.L. Larsson, F. Hild, "Granite rock fragmentation at percussive drilling – experimental and numerical investigation", International Journal of Numerical and Analytical Methods in Geomechanics, vol. 38, pp. 828-843, 2014, https://doi.org/10.1002/nag.2235

[4] T. Saksala, "3D numerical modelling of bit-rock fracture mechanisms in percussive drilling with a multiple-button bit", International Journal of Numerical and Analytical Methods in Geomechanics, vol. 37, pp. 308-324, 2013, https://doi.org/10.1002/nag.2173

[5] T. Saksala, "Numerical study of the influence of hydrostatic/confining pressure on percussive drilling of hard rocks", Computers and Geotechnics, vol. 76, 120128, 2016, https://doi.org/10.1016/j.compgeo.2016.02.021

[6] T. Saksala, D. Gomon, M. Hokka, M., V.-T. Kuokkala, "Numerical and experimental studies of percussive drilling with a triple-button bit on Kuru granite", International Journal of Impact Engineering, vol. 72, pp. 56-66, 2017, https://doi.org/10.1016/j.ijimpeng.2014.05.006

[7] M. Hokka, J. Black, D. Tkalich, M. Fourmeau, A. Kane, N.H. Hoang, C.C. Li, W.W. Chen, V.-T. Kuokkala, "Effects of strain rate and confining pressure on the compressive behavior of Kuru granite", International Journal of Impact Engineering vol. 91, pp. 183-193, 2016, https://doi.org/10.1016/j.ijimpeng.2016.01.010

[8] D. Tkalich, M. Fourmeau, A: Kane, C.C. Li, G. Cailletaud, "Experimental and numerical study of Kuru granite under confined compression and indentation", International Journal of Rock Mechanics and Mining Science, vol 87 pp. 55-68, 2016, https://doi.org/10.1016/j.ijrmms.2016.05.012

[9] T. Saksala, M. Hokka, V.-T. Kuokkala, "Numerical 3D modelling of the effects of strain rate and confining pressure on the compressive behavior of Kuru granite", Computers and Geotechnics, vol. 88, pp. 1-8, 2017, https://doi.org/10.1016/j.compgeo.2017.03.004

[10] S. Dumoulin, I. Thenevin, A. Kane, A. Rouabhi, J.-P. Latham, E. Jahangir, G. Vistnes, H. Sellami, "A complete experimental study on hard granites: microstructural characterization, mechanical response, and failure criterion", ongoing work

[11] K. Liu, Q.B. Zhang, J. Zhao, "Dynamic increase factors of rock strength", Proceedings of the 3rd International Conference on Rock Dynamics and Applications, ROCDYN-3, CRC Press, pp. 169-174, 2018

[12] H.A. Aldannawy. "Le forage percussif en conditions extrêmes : expérimentations et modélisations numériques". PhD thesis of Ecole des Mines de Paris, 2022, https://pastel.hal.science/tel-03947276v1

[13] M. Andersson, J.J.E. Lie, and E.S. Husebye, "Tectonic setting of post-orogenic granites within SW Fennoscandia based on deep seismic and gravity data", Terra Nova, vol. 8(6), pp. 558-566, 1996, https://doi.org/10.1111/j.1365-3121.1996.tb00785.x

[14] Abaqus: Damaged plasticity model for concrete and other quasi-brittle materials, Theory Manual, Dassault Systèmes Simulia Corp., 2022

[15] J. Lubliner, J. Oliver, S. Oller, and E. Oñate, "A Plastic-Damage Model for Concrete", International Journal of Solids and Structures, vol. 25, pp. 299–329, 1989, https://doi.org/10.1016/0020-7683(89)90050-4

[16] J. Lee, and G.L. Fenves, "Plastic-Damage Model for Cyclic Loading of Concrete Structures", Journal of Engineering Mechanics, vol. 124(8), pp. 892–900, 1998, https://doi.org/10.1061/(ASCE)0733-9399(1998)124:8(892)

[17] N. Stander, A. Basudhar, W. Roux, K. Liebold, T. Eggleston, T. Goel, K. Craig. LS-OPT user’s manual, Version 7.0. Livermore Software Technology Corporation, 2020

[18] H.A. Aldannawy, A. Rouabhi, L. Gerbaud, "Percussive Drilling: Experimental and Numerical Investigations", Rock Mechanics and Rock Engineering, vol. 55, pp. 1555–1570, 2022, https://doi.org/10.1007/s00603-021-02707-5

Appendix A. Effect of mesh size

The mesh size used in the calibration of the model was different from the one used for the different drill bit-rock interaction studies done in the current Section 4. The effect of the mesh size was investigated by running the simulation of a model with a finer mesh. The configuration chosen was the flat profile with 10 mm deep groove and all other boundary conditions as stated in section 4.1, i.e.: constant pressure of 100 MPa on external horizontal and vertical walls, constant pressure of 40 MPa on bottom-hole, inner walls and groove walls, initial internal stress of 100 MPa on the rock. The inserts were meshed with about 199,660 rigid elements, R3D4 and R3D3, and the rock was discretized with about 4,726,909 quadratic tetrahedral elements, C3D10M. Here, the tetrahedral elements in the impact area on the rock had an edge length of about 1 mm. Figure 33(a) and (b) show the full element model and a close-up revealing the fine mesh used.

Figure 34(a) and (b) show the accumulated damage, with a 0.85 threshold, for both mesh sizes. Although not identical, the distributions are very similar. Figure 35(a) and (b) show the force versus penetration curves and volume removed, respectively, for both mesh sizes. Very similar force versus penetration curves and volume removed are obtained thus indicating that the 3 mm mesh size provides valid results. Note that the simulation with a 1 mm mesh size took about 33 hours to run on a Linux workstation, while the 3 mm mesh size took about one hour; both were run on the same workstation using the same number of processors.

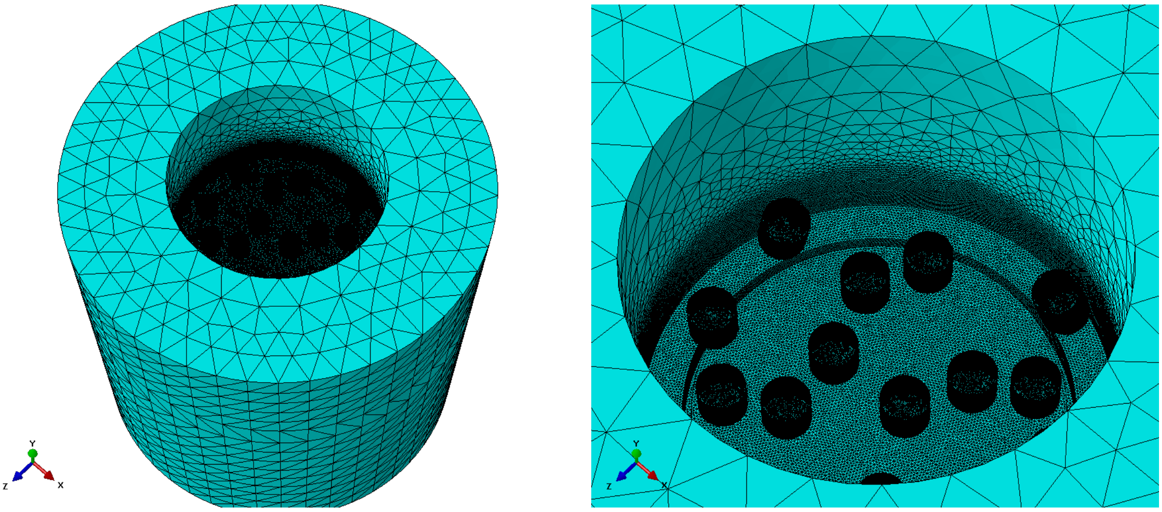

(a) (b)

Figure 33: (a) View of the fine full finite element model, (b) close-up.

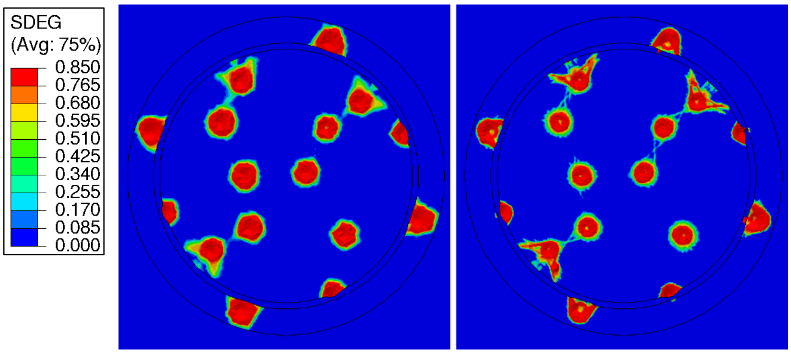

(a) (b)

Figure 34: Contour plots of accumulated damage for a (a) 3 mm and (b) 1 mm mesh size.

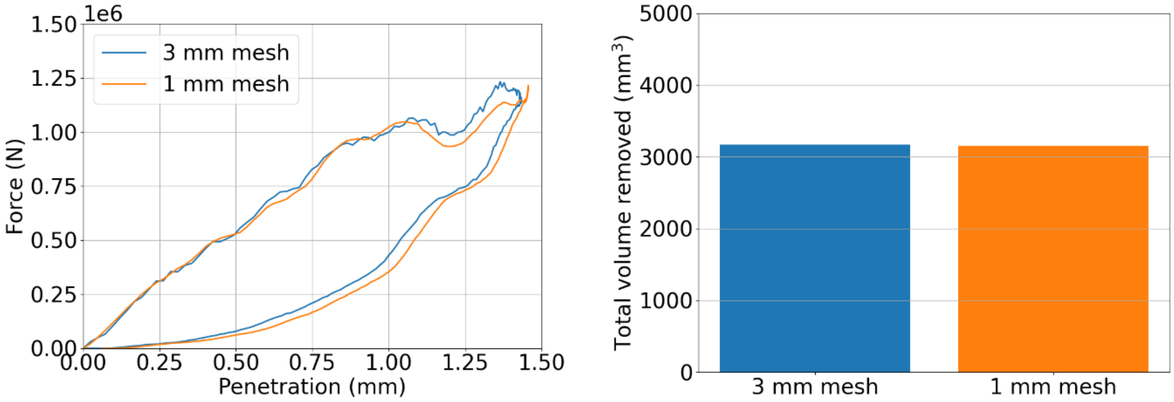

(a) (b)

Figure 35: (a) Force versus penetration curves and (b) volume removed, for different mesh sizes.

Appendix B. Effect of heterogeneity

An example of how heterogeneity can be accounted for is briefly described here. This is only a demonstrator which has been built independently of the homogeneous approach.

Based on nano-indentation tests performed on Sidobre granite at Imperial College London, the concrete damaged plasticity (CDP) model has been calibrated for each phase, i.e., feldspar, quartz and biotite. Assuming such calibration is independent of the grain size and volume fraction, it can then be applied to any granite. Then, using the flat profile geometry with a 10 mm deep groove, a random distribution of the phases for the Red Bohus granite was generated. Each element of the mesh was attributed a phase, while respecting the volume fraction of each phase, i.e., 60% feldspar, 35% quartz and 5% biotite. Heterogeneity was accounted for only underneath the drill bit since plasticity and damage only occur in that volume; the remainder of the rock was modelled as homogeneous, see Figure 36.

A simulation was run with multiple impacts, such that a full rotation of the drill bit was obtained. The boundary conditions were the same as those described in section 4.1. The accumulated damage after one impact, 10 impacts and a full rotation of the drill bit are shown in Figure 37(a), (b) and (c), respectively. A threshold of 0.85 is used. Although the rock is heterogeneous, it clearly appears that the damage is generally homogeneously distributed.

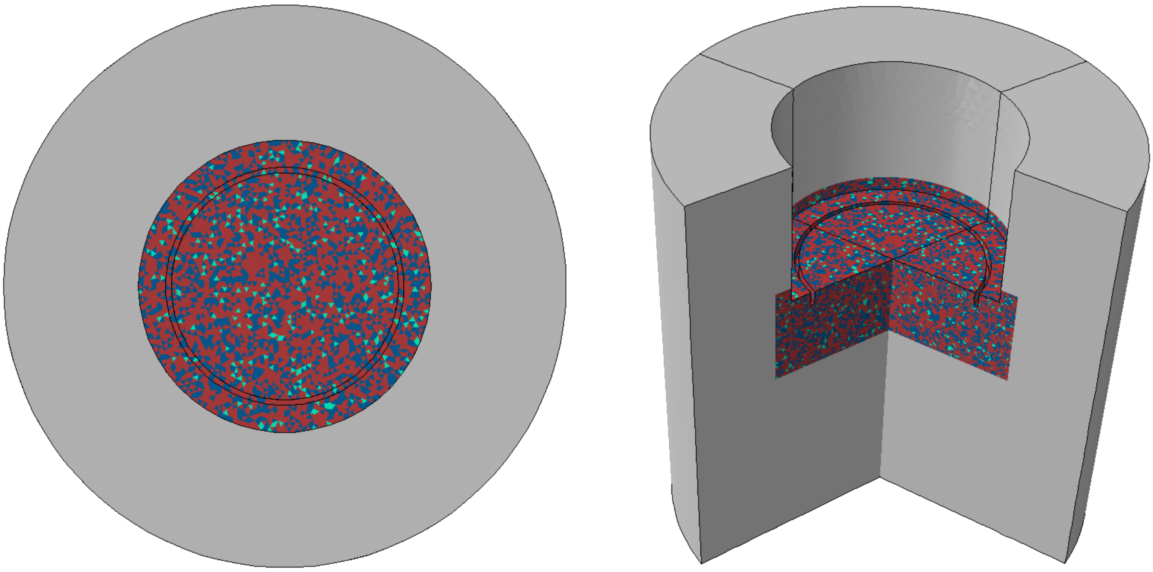
(a) (b)

Figure 36: Distribution of the phases in the volume: elements in red, blue and green correspond to feldspar, quartz and biotite, respectively, while grey is the homogeneous material.

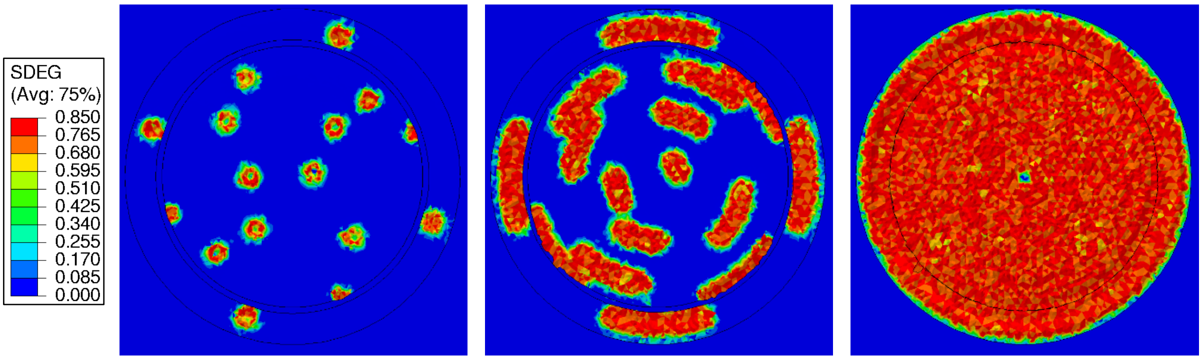

(a) (b) (c)

Figure 37: Contour plots of accumulated damage after (a) 1 impact, (b) 10 impacts, and (c) a full rotation.